Applied Surface Science 612 (2023) 155949

Contents lists available at ScienceDirect

Applied Surface Science

journal homepage: www.elsevier.com/locate/apsusc

Full Length Article

Electrospinning near infra-red light-responsive unzipped CNT/PDA nanofibrous membrane for enhanced antibacterial effect and rapid drug release

Tejal V. Patil [a,b], Sayan Deb Dutta [a], Dinesh K. Patel [c], Keya Ganguly [a], Ki-Taek Lim [a,b,c,*]

[a] Department of Biosystems Engineering, Kangwon National University, Chuncheon 24341, Republic of Korea
[b] Interdisciplinary Program in Smart Agriculture, Kangwon National University, Chuncheon 24341, Republic of Korea
[c] Institute of Forest Science, Kangwon National University, Chuncheon 24341, Republic of Korea

ARTICLE INFO

Keywords:
Unzipped CNT
Mussel-inspired
Electrospinning
Antibacterial platforms
Antibiofilm
Drug delivery

ABSTRACT

Presently, efficient protection from bacterial infections is considered a potential threat owing to the raise of multidrug resistant bacterial phenotypes. Hence, there is an urgent requirement to develop alternative strategies for eliminating bacterial infections. In this regard, near infra-red (NIR) responsive photothermal agents (PTAs) has received significant attention. We report a mussel-inspired NIR-responsive unzipped CNT (uCNT)-based nanocomposite to combat against bacteria. The modification of mussel-inspired polydopamine (PDA) coating improved the NIR responsiveness and biocompatibility of uCNTs. The temperature of uCNT@PDA increased by 40 °C upon exposure of 808 nm NIR light (1.0 W/cm^2, 10 min) showing the excellent photothermal property. PCL/uCNT@PDA nanofiber mats showed controlled photothermal heating upon low power density (0.5 W/cm^2) NIR irradiation and exhibited robust mechanical strength up to 20 MPa (PCL/uCNT@PDA-1). Taking advantage of photothermal effect and ROS generation, the nanofiber displayed remarkable antibacterial efficacy against *Bacillus subtilis* (gram positive) and *Escherichia coli* (gram negative) and displayed the release of curcumin in presence of NIR light. The fabricated PCL/uCNT@PDA platform is bioactive, anti-oxidative, and non-toxic for human dermal fibroblast cells. Therefore, we anticipate that the developed uCNT@PDA is a potential PTA and the fabricated nanofiber may provide a versatile platform for eradicating bacterial contamination in medical and non-medical sectors.

1. Introduction

Bacteria are well known for their ability to adapt and reproduce in any environment. They can cause severe infections by entering the body through contaminated water, edible items, and biomedical equipment [1]. To eradicate bacterial infections, more effective and safe treatments must be developed and employed in practice. In the last few years, near-infrared (NIR) light–induced photothermal and ROS generation effects on antibacterial activity have been recognized as promising strategies [2–7]. These photothermal materials are excited upon exposure to light at a suitable wavelength, generating vibrations in the lattice to produce heat. The heat generated can rupture bacterial membranes and protein structures [8–10]. To date, considerable efforts have been dedicated to synthesizing NIR-responsive materials and determining their applications in antibacterial and photocatalytic material synthesis, drug delivery, cancer treatment, bioimaging, shape memory polymer synthesis, sterilization of surfaces and 4D printing. However, an important precaution to consider while treating human cells with NIR-responsive materials is that the power density should not harm the human cells and surrounding environment. NIR light (NIR-I, 650–950 nm; NIR-II, 1000–1700 nm) has a high tissue penetration depth and low absorption in the blood and body water of organisms [11]. He et al. suggested that when light-sensitive materials are exposed to a specific wavelength of light, these materials can generate a large number of electron-hole pairs, resulting in the production of hydroxyl radicals (•OH), singlet oxygen ($^1O_2$), or superoxide radicals ($\bullet O_2^-$), which can effectively kill bacteria by interfering with the metabolic pathways [12]. The integration of multiple bacterial killing strategies, such as heat production and ROS generation, has been considered beneficial in many ways. These mechanisms can improve bactericidal efficiency, reduce the time

* Corresponding author at: Department of Biosystems Engineering, Kangwon National University, Chuncheon 24341, Republic of Korea.
E-mail address: ktlim@kangwon.ac.kr (K.-T. Lim).

https://doi.org/10.1016/j.apsusc.2022.155949
Received 23 September 2022; Received in revised form 18 November 2022; Accepted 29 November 2022
Available online 5 December 2022

required to kill bacteria and the need for repeated doses of antibacterial agents. Recently, some composite structures, including Au NBPs@SiO_2 [13], MoS_2-PEI [14], Au@Ag NPs [15], and TiO_2-FeS_2 [16], have been fabricated, and their NIR-responsive properties and antibacterial activities have been studied. Nevertheless, these expensive metal-based materials have limited advantages owing to their high cost and the environmental issues caused by the use of these metals. In addition, noble and precious metals are expensive due to their limited availability.

In this regard, carbon nanotubes (CNT) are cheaper and widely considered one of the ideal materials for biomedical research and related applications owing to their high surface area, high aspect ratio, and impressive material properties, such as mechanical strength and thermal and electrical conductivity, which are favorable for the bulk-scale manufacture of next-generation composite materials [17]. Due to these distinctive properties, CNT has been extensively used in biomedical, electrical, energy, and water purification applications [18–20]. CNT has a long history of antibacterial activity [21]. The antibacterial effect of CNTs has already been studied in gram-positive and gram-negative bacteria, such as *Staphylococcus aureus* and *Pseudomonas aeruginosa* [22,23]. Functionalization can alter the properties of pristine CNT. Unzipping of multiwalled CNT (MWCNT) can be used as a hybrid carbon material with improved CNT properties. The procedure for the horizontal unzipping of CNT was previously reported by Mondal et al. [24]. These carbon materials have been widely used in the energy sector. However, the NIR-responsive properties of unzipped carbon nanotubes (uCNT) have not yet been substantially explored. Hence, there is scope for further investigation and utilization. In a recent study [20], the potential and applicability of uCNT in tissue engineering were studied, and these materials exhibited enhanced osteogenic properties. Bacterial eradication and NIR properties of uCNTs are yet to be explored.

Since the decade, NIR properties of carbon materials such as CNT, graphene oxide (GO), and reduced graphene oxide (rGO) have been explored. Several studies have been published stating that these carbon materials are NIR sensitive and applicable in bio-imaging, cancer treatment, drug delivery, and bacteria-killing [25]. Table 1 presents the literature on carbon composites with their NIR properties and applications. Recently, Nguyen et al. [26] studied the photothermal properties of water-soluble MWCNT. The 60.0 mg/L sample showed a maximum NIR effect. The temperature increased to 66.4 ± 0.2 °C after 30 min of 808 nm NIR light irradiation. In another study, NIR effect of GT-DA/CS/CNT composite was examined for the application of bacteria infected skin regeneration [27]. The composite displayed 17.2 °C and 23.3 °C temperature differences for 1 wt% and 4 wt% CNT-PDA concentration after irradiating 808 nm NIR light for 10 mins. Nonetheless, the temperature required to kill bacteria should be more high which can be regulated by time exposure and concentration. In order to overcome this drawback, we developed PCL/uCNT@PDA nanofibers which showed remarkable results against bacteria. The temperature achieved by NIR exposure of our fabricated material was enough to kill bacteria. PCL and polydopamine were selected depending upon their biocompatibility.

Table 1
A comparative study of some previously reported NIR responsive systems demonstrating their advantages and limitations with our developed system.

System	Conc.	Laser Power (W/cm^2)	Time (min)	Temp (°C)	Advantages	Limitations	Ref.
PAA@rGO	4 mg/ml	1.0 (980 nm)	5	67	Antibacterial, and wound healing	Mechanical strength of material not performed relatively slow increase in temperature, and high concentration	[33]
GT-DA/CS/CNT	4 wt% CNT-PDA	1.0 (808 nm)	10	49.2	Antibacterial, and wound healing	Relatively slow enhancement in temperature after NIR irradiation	[27]
$DQ_{0.5}C_1$	1% CNT and 0.5% QCGM in DEA	1.6 (808 nm)	4	73.8	Antibacterial, and wound healing	Relatively high power density	[64]
Thermogel rGO	10 μg/ml	1.7 (808 nm)	10	8.1 (ΔT)	Cancer therapy, Bacteria killing	Mechanical and thermal strength not performed, and relatively slow enhancement in temperature	[65]
PU-EDM/rmGO	2 wt% rmGO	1.0 (808 nm)	1	150	Soft robotics	Thermal strength and biocompatibility not performed	[66]
CNTs-PAMAM-Ag_2S	1 mg/ml	1.0 (980 nm)	7	62.4	Efficient enhancement in temperature	Mechanical, and thermal strength not performed, Biocompatibility not shown	[67]
PCL/uCNT@PDA-1	1% uCNT@PDA	1.0 (808 nm)	5	115	**Improved mechanical and thermal strength, rapid enhancement in temperature sustained drug release, biocompatible, antioxidant, andsuperior antibacterial potentials**		**Present study**

Abbreviations: Poly (acrylic acid)-PAA, reduced graphene oxide-rGO, gelatin-GT, dopamine- DA, chitosan-CS, carbon nanotube-CNT, glycidyl methacrylate functionalized quaternized chitosan-QCGM, *N*,*N*-diethylacrylamide-DEA, Polyurethane-PU, hydrazine hydrate modified maleimide functionalized graphene oxide-rmGO, Poly(*N*-isopropylacrylamide)-PNIPAAm, Liquid crystal elastomer-LCE.

Polydopamine is synthesized from monomer dopamine which is an important material within the marine mussel adhesive protein. It can undergo non-covalent self-assembly and oxidative self-polymerization under weak and basic conditions. Moreover, an intramolecular Michael addition reaction could lead to the formation of a cross-linked polydopamine homopolymer [28,29]. PDA also has good biocompatibility and shows a strong photothermal effect under stimulus of near-infrared (NIR) light [30]. In past few years, the potential of PDA in free radical scavenging, UV shielding, photothermal conversion has been highly explored [31,32]. However, within our knowledge, the potential of unzipped CNT with polydopamine has not been yet explored in the arena of NIR properties.

Altinbasak et al. [33] prepared PAA@rGO nanofiber composed of rGO and poly(acrylic acid) to apply "on-demand" Ampicillin and Cefepime release. The material showed better wound healing in bacteria-infected mice due to NIR-responsive Ampicillin and Cefepime release. However, the NIR effect for bacteria-killing was not studied. In the present study, the bacteria-killing effect of fabricated material PCL/uCNT@PDA was demonstrated in presence of NIR. Additionally, curcumin, which is well known for its antibacterial property, can enhance the bacteria killing. It is anticipated that PCL/uCNT@PDA itself kills bacteria in presence of NIR light, but addition of curcumin can enhance the property.

Stimuli-responsive materials are well-known smart materials with unique properties that can be used in biomedical fields [34,35]. Light is an ideal stimulus to be applied remotely, focused accurately, and switched rapidly among various stimuli, such as magnetic field, pH, electric field, and pressure. Though, electrospun PCL scaffolds reinforced with uCNT@PDA have not yet been studied, particularly for NIR-responsive antibacterial and drug delivery applications. This study examined the synergetic effects of uCNT and PDA on NIR responses. This study aimed to fabricate mechanically strong PCL/uCNT@PDA platforms using the electrospinning technique and, more importantly, study the NIR effect on bacterial killing and drug delivery. The biocompatibility with the skin cell line was also analyzed, showing the potential of PCL/uCNT@PDA nanofibers in medical applications.

The drug, curcumin, is a nature-derived compound that is very effective; but, it has weak aqueous solubility and low bioavailability, which could limit its further applications [36]. Thus, an efficient drug delivery carrier need to be designed for curcumin delivery. This study focuses on creating NIR light-responsive surfaces and analyzing their potential for antibacterial and drug delivery applications (Scheme 1). The developed hybrid PCL/uCNT@PDA nanofibers were successfully designed with curcumin drug to understand the drug-release behavior of the nanofibers. The hybrid material was the most appropriate system for sustained release of curcumin in the presence and absence of NIR light. In addition, detailed characterizations, morphological investigations, and antibacterial properties of the PCL/uCNT@PDA nanofibers were extensively investigated. Moreover, by selecting human dermal fibroblasts (HDF) as model cell lines, the cytotoxicity of nanofibers was examined to explore the potential of the fabricated nanofibers in the biomedical field.

2. Experimental section

2.1. Materials and reagents

All the chemicals were used as received unless stated. Multiwalled CNTs (MWCNT) were received from Applied Carbon Nano (ACN) (Republic of Korea). The reagents Sulfuric acid (H_2SO_4) (95.0%), hydrochloric acid (HCl) (35.0%), and hydrogen peroxide (H_2O_2) (30%) were purchased from Wako Chemicals (Republic of Korea). Potassium permanganate ($KMnO_4$) and dimethylformamide (DMF) were purchased from Daejung chemicals (Republic of Korea). The chemicals such as Dopamine hydrochloride, Tris(hydroxymethyl) aminomethane (Tris buffer), curcumin, 5,5-Dimethyl-1-pyrroline *N*-oxide (DMPO), and sodium nitrate were purchased from Sigma-Aldrich (USA). The Polycaprolactone (PCL; ≥95%, Sigma-Aldrich, USA; CAS: 24980–41-4) with an average molecular weight of 80,000 g/mole was used for preparing the PCL/uCNT@PDA composites. Tween 20 was received from BIO-

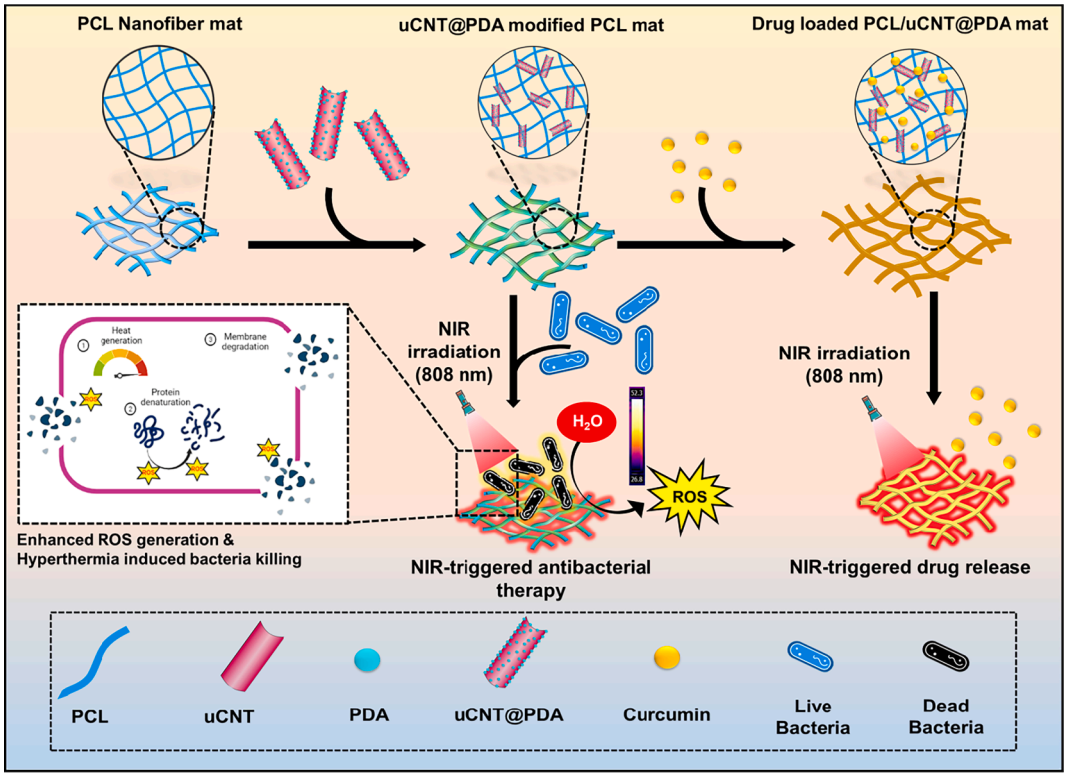

Scheme 1. Synthesis of uCNT@PDA nanofiber and NIR effect on bacteria killing and drug delivery in the presence of NIR light source.

RAD, Republic of Korea.

2.2. Synthesis of unzipped MWCNT (uCNT)

Synthesis of uCNT was performed with reference to the previously reported procedure [37]. In brief, 1.0 g of MWCNTs were dispersed in the mixture of 100 ml sulfuric acid and 10.0 g sodium nitrate and agitated for 2 h in an ice bath. Next, 5.0 g of potassium permanganate was gradually added to the resultant mixture. As per the report of Kosynkin et al. [38], unzipping of CNTs initiates by the addition of $KMnO_4$ in a concentrated H_2SO_4 solution in hot conditions. Unzipping of MWCNTs can be regulated by breaking of internal C—C bonds of MWCNTs, followed by further sequential stretching and breaking [39]. Further, the resultant solution was treated at 70 °C under continuous stirring for 2 h. In order to avoid precipitation of manganese oxide, the oxidized materials were treated with a hydrogen peroxide solution, followed by repeated washing with distilled water. The acquired solid product was dried for 48 h in a hot air oven at 50 °C. MWCNT was successfully unzipped using the above procedure and denoted as uCNT.

2.3. Preparation of uCNT@PDA

Fabrication of polydopamine (PDA) with uCNT was performed by using the previously reported procedure [40], by keeping a 1:1 wt ratio of uCNT and dopamine hydrochloride. In this synthesis, uCNT powder (0.5 g) was dispersed into Tris buffer solution (100 ml, 10 mM, pH 8.5) by using ultrasonication. After homogenous dispersion of uCNT, dopamine hydrochloride (0.5 g) was added to the dispersion and stirred at room temperature overnight. The synthesized uCNT@PDA were separated from the reaction mixture by centrifugation at 8000 rpm for 10 min. The resultant product was further washed with distilled water and ethanol three times and dried at 40 °C overnight.

2.4. Preparation of electrospun nanofiber

Polycaprolactone with an average molecular weight of 80,000 g/mol was used to prepare the PCL/uCNT@PDA nanofibers. In this study, different concentrations of PCL/uCNT@PDA nanofibers were synthesized using varying amounts of uCNT@PDA (0.25%, 0.5%, and 1% w/v). The desired amount of uCNT@PDA was dispersed in dimethylformamide (DMF) by ultrasonication to obtain a homogeneous black dispersion. Furthermore, 15% (wt.%) PCL solution was prepared by adding PCL in DMF solvent at 70 °C with continuous agitation. After the preparation of a homogeneous mixture of PCL, uCNT@PDA dispersions (0.25%, 0.5%, and 1%) were added dropwise to the PCL solution and the resultant mixture was kept under stirring conditions till a homogeneous mixture was obtained. Electrospinning of the PCL/uCNT@PDA solution was performed using an electrospinning device, PCL/uCNT@PDA was loaded into a 10 cm^3 plastic syringe, and the collector was wrapped with aluminum foil for ease of removal of the nanofibers. The polymer solution was pumped through the syringe using a 21-gauge needle at a constant flow rate of 2.0 ml/h and 16.0 kV/cm voltage. The distance between the collector roller and needle tip was maintained at approximately 15 cm. The electrospun mats were prepared at room temperature with 40–50% humidity. The fabricated nanofibers were named PCL, PCL/uCNT@PDA-0.25, PCL/uCNT@PDA-0.5, and PCL/uCNT@PDA-1, depending on the amount of uCNT@PDA added.

2.5. Preparation of PCL/uCNT@PDA-Cur

In this study, 3% curcumin was added to the PCL/uCNT@PDA solution and stirred overnight to obtain a homogeneous solution. The resultant samples were electrospun using parameters similar to those of the aforementioned parameters. The prepared nanofibers were denoted as PCL/uCNT@PDA-Cur.

2.6. Characterization

Characterization of synthesized material was conducted to confirm the morphology and physicochemical properties using traditional characterization techniques. Morphology and structural properties of MWCNT, uCNT, and uCNT@PDA were examined through transmission electron microscopy (TEM, JEM2100F, Jeol, Japan) and collected quality TEM images. In addition, the morphology of fabricated samples and nanofiber were evaluated through scanning electron microscopy (FE-SEM; Hitachi S-4800, USA). Elemental composition in uCNT and uCNT@PDA was confirmed through EDS mapping analysis. X-ray Photoelectron Spectroscopy (XPS, K Alpha$^+$, ThermoFisher, USA) analysis was additionally performed to confirm the elemental composition and binding energies. Fourier transform infrared spectroscopy (FTIR, Perkin-Elmer, UK) was used to investigate functionalization (bonding information) between organic functional groups in the samples. Mid-infrared region (4000–500 cm^{-1}) was used to collect the FTIR spectrum. The desired functionalization was also confirmed through the Raman spectroscopy technique (SENTERRA) by analyzing non-functionalized and functionalized materials using an excitation wavelength of 532.04 nm. Raman spectroscopy was conducted to study the defects and graphitization structure of carbonaceous materials and further confirm the structural change in the unzipping process. X-ray diffraction patterns (XRD) were recorded using Panalytical, X'pert Pro diffractometer in the range of 15-30° using Cu Kα radiation. The zeta potential of the dispersions was determined through a dynamic light scattering analyzer (Malvern Palanytical ZSP) at a temperature of 25 °C. Characterization of PCL/uCNT@PDA nanofibers was also performed by FE-SEM, FTIR, and XRD following the previously mentioned parameters. The thermal stability of prepared materials was evaluated through a thermogravimetric analyzer, and the sample was analyzed under a nitrogen atmosphere at a heating rate of 10 °C/min from 30 to 800 °C. A thick film of PCL and PCL/uCNT@PDA was prepared to analyze the mechanical properties. Tensile test was performed by Universal Testing Machine (UTM; MCT-1150, AND Inc., Japan) using a constant speed of 10 mm/min. The hydrophilicity of electrospun nanofibers was evaluated using a static contact angle instrument (Phoenix-MT). Contact angles, indicating surface wettability, were calculated by depositing deionized water droplets directly on the membrane surface.

2.7. Degradation study

To analyze the degradation of PCL composite nanofibers, all four nanofibers were cut into 15 × 5 mm^2 pieces and immersed in 5 ml of 0.1 mM NaOH solution. Test tubes were placed in a water bath at 37 °C under shaking conditions. Each of the four nanofibers was removed from the NaOH solution at predetermined intervals. The nanofibers were cleaned with deionized water and dried in a hot air oven. The weight of the dried samples (W_t) was recorded, and the mass loss (W) of the samples was calculated using the formula:

$$W = \frac{W_i - W_t}{W_i} \times 100 \quad (1)$$

Where W_i is the initial weight of each sample.

2.8. Antioxidant efficiency of membranes

The antioxidant efficiency of specimens was tested by measuring their capacity to scavenge the stable 2, 2-diphenyl-2-picrylhydrazyl (DPPH) free radical, using the previously mentioned protocol [41]. Typically, 1.0 mg of prepared nanofibers were added to 500 μL of 100 μM DPPH (100 × 10^{-6} M) solution in ethanol. Further, the mixture was incubated in the dark for 30 min. Then, the wavelength scanning was performed using a UV–vis spectrophotometer (Infinite® M Nano 200 Pro; TECAN, Switzerland) at 517 nm. The DPPH degradation was

calculated using the following equation.

$$DPPHscavenging = \frac{A_B - A_S}{A_B} \times 100\% \quad (2)$$

Where A_B and A_S are the absorbance values of the blank (DPPH + ethanol) and the samples (DPPH + ethanol + sample), respectively.

2.9. In vitro photothermal performance

The in vitro photothermal performance of uCNT, uCNT@PDA, and PCL/uCNT@PDA nanofibers was systematically studied by exposing the nanofiber to 808 nm NIR laser light. Different concentrations of uCNT dispersions in water were used to evaluate the photothermal properties. The real-time temperature was recorded at 30 s, followed for every 1 min interval up to 5 min. The photothermal effects of the uCNT, uCNT@PDA, and nanofibers were studied by irradiation with two different laser powers (0.5 and 1.0 W/cm^2).

2.10. Drug delivery

The PCL/uCNT@PDA-Cur nanofibers were immersed in buffer solution (2% Tween 20 in PBS) at pH 7.4. At determined time intervals, the medium was collected for UV–vis analysis and immediately replaced with a fresh buffer solution. In order to study NIR-triggered drug release behavior, the PCL/uCNT@PDA-Cur nanofibers with equal weight were immersed in buffer at pH 7.4. Drug release was recorded with and without NIR irradiation. To determine the NIR effect on drug delivery, the laser light was irradiated to the samples in buffer solution prior to every reading recorded at a particular interval of time. The released curcumin was collected for UV–vis analysis. The accumulative released drug was calculated using

$$Drugrelease(\%) = \frac{D_{released}}{D_{total}} \times 100\% \quad (3)$$

Where $D_{released}$ is the total amount of released Curcumin and D_{total} is the amounts of drug incorporated in the nanofibers. The content of released curcumin was calculated according to the calibration curve at different concentrations (**Figure S1**). The above experiment was repeated (n = 3) for accurate analysis.

2.11. In-vitro antibacterial activity assay

In vitro antibacterial assays were conducted on the basis of standard antibacterial protocols [42]. As representatives, Gram-positive *Bacillus subtilis* (*B. subtilis*) and Gram-negative *Escherichia coli* (*E. coli*) were adopted in current tests. All strains were tested in three separate experimental groups, including PCL and all PCL/uCNT@PDA samples with and without NIR (n = 3 for each experimental group). Both *B. subtilis* and *E. coli* bacteria were cultured aerobically at 37 °C for overnight in sterile nutrient broth, and the bacterial concentration was determined prior to use. The samples to be tested were sterilized under ultraviolet light for 1 h before being transferred to a well plate. All membranes were immersed in 12-well culture plates containing 1.0 ml of bacterial suspension (OD_{600} = 0.1). Then the treatment set was irradiated with 808 nm NIR light for 10 min and incubated for 1 h. An additional group was treated in the same way without irradiation as a control group. Later, the suspension was cultured on agar plates at 37 °C for overnight to observe the number of colonies. The antibacterial property was determined by the number of colonies counted. To observe the morphology of NIR-treated cells, bacteria were fixed with a 1:1 ratio of 2.5% glutaraldehyde and 2.5% paraformaldehyde. Further, the bacteria were dehydrated with serial concentrations (10, 30, 50, 70, 80, 90, and 100%) of ethanol solutions. Later, the cells were spread on mica films, allowed to dry, and stored it at 4 °C till analysis. Before analysis, samples were gold-sputtered for SEM examination.

2.12. Anti-biofilm activity

In order to examine the antibiofilm activity, similar bacteria, i.e., *B. subtilis* and *E.coli,* were used. Prior to the experiments, the samples were cut into equal dimensions and treated under UV rays for sterilization. Nanofiber mats were then transferred into sterile 24 well plates, each well containing 1 ml of sterile nutrient broth culture medium. A volume of 150 μL from the cultures (OD_{600} = 0.1) of *B. subtilis* and *E. coli* was added to the wells separately, containing nutrient broth. Plates were further incubated at 37 °C for the formation of biofilm development. After the required formation of biofilm, the cultures were treated with NIR light, and nanofibers without NIR treatment were utilized as a control.

For quantitative analysis, the nanofibers with and without NIR treatment were carefully transferred to new 24 well plates, and quantification was performed using crystal violet assay. Biofilms formed on nanofiber mats and wells were gently rinsed with sterile PBS buffer (pH 7.4, three times). Biofilms were stained with 0.4% crystal violet (500 μL) dye at room temperature for 15 min. Stain in the wells and on nanofibers was gently washed with PBS buffer (three times) to remove unbound and excess color. The crystal violet retained by the biofilm on nanofiber was solubilized in 500 μL of 33% acetic acid, and the absorption was measured at 620 nm. The stain retained in the wells was air-dried in the oven after washing to capture the images.

2.13. In vitro assay

2.13.1. Cell culture

Human dermal fibroblasts (HDF) (ATCC No. PCS-201–012) cells were cultured in DMEM media supplemented with 10% FBS and 1% P/S antibiotics. Subsequently, HDF cells were grown to confluence and then detached by trypsinization and counted by using a hemocytometer prior to seeding on samples.

2.13.2. Cytotoxicity of nanofibers

The cell viability of HDF cells was assessed on fabricated nanofibers (PCL, PCL/uCNT@PDA-0.25, PCL/uCNT@PDA-0.5, and PCL/uCNT@PDA-1 in order to compare their biocompatibility. The nanofibers were cut into 0.5 × 0.5 cm and placed into 96 well culture plates. The samples were UV treated before utilization. 1.5 × 10^4 cells/well were seeded onto the samples in a 96-well culture plate. The viability was checked on 1, 3, and 5 days after the cell seeding on nanofibers. Cells seeded on PCL nanofibers were considered as control. For the analysis, old media was replaced with fresh media (100 μL), and WST-8 (10 μL) dye was added to each sample and incubated for 2 h to form formazan at 37 °C. WST-8 kit solution contains tetrazolium salt, which converts into orange formazan dye in the presence of live cells. Therefore, more number of live cells will produce a high quantity of formazan dye which helps to analyze the cell viability. After incubation of 2 h, the optical density of samples was measured at 450 nm wavelength by UV–vis spectrophotometer (Infinite® M Nano 200 Pro; TECAN, Switzerland). The results of PCL/uCNT@PDA-0.25, PCL/uCNT@PDA-0.5, and PCL/uCNT@PDA-1 samples were compared with control (PCL). All the results were performed in triplicate (n = 3), and data is shown at mean ODs ± standard deviations.

2.13.3. Live/Dead assay

Sterilized nanofiber mats were inserted into 96-well plates, and HDF cells (1 × 10^4 cells/well) were cultured upon them and incubated at 37 °C. The cells were allowed to grow in DMEM media for 3 and 6 days. For the analysis, cells were washed with 1X PBS and treated with 1 μL of acridine orange and ethidium bromide dye solution at 1:1 ratio. Images were captured on day 3 and day 6 by an inverted fluorescence microscope (DMi8 Series, Leica Microsystems, Germany).

2.14. Statistical analysis

Statistical analysis was calculated by utilizing OriginPro 9.0 software. Statistical significance between control and treatment sets was determined using one-way ANOVA. The data are presented as mean ± standard deviations (SDs). Differences were considered significant at *p < 0.05, **p < 0.01, ***p < 0.001.

3. Results and discussion

3.1. Characterization of uCNT and uCNT@PDA

The synthesis of uCNT@PDA is shown schematically in Fig. 1**(a)**. The uCNT was successfully synthesized from the MWCNT using a one-pot synthesis approach. The synthesis was confirmed using characterization techniques. Fig. 1**(b)** shows TEM images of the MWCNT, uCNT, and uCNT@PDA. The characteristic hollow MWCNT tubes with long intact rods were observed. Similar results have been reported in previous studies [43]. The wall of the MWCNT was opened after the unzipping treatment by oxidation to obtain uCNT. However, the obtained TEM results indicate that the synthesized uCNT has a high aspect ratio. The change in the TEM image of the PDA-modified uCNT indicates the deposition of the PDA coating on the uCNT structure. The morphologies of the MWCNT, uCNT, and uCNT@PDA were confirmed using the SEM (Fig. 1**(c)**) analysis, where the cutting of the MWCNT into uCNT was clearly observed. Random domains of uCNT were visible, which is strong evidence for the successful unzipping of the MWCNT. In the SEM image of uCNT@PDA, the agglomeration of organic moieties was evident. The PDA molecules were homogenously dispersed and concentrated on the uCNT surface. Elemental dispersion was obtained using the EDS mapping analysis (Fig. 1**(d)**), all the oxygen moieties were observed to be significantly located and well-dispersed on the surface. The sum spectrum (**Figure S1**) of the EDS mapping is provided in **Table S1**. However, even dispersions of C, N, and O were observed in the EDS mapping images. This indicates that the improved oxy-functional groups in uCNT favored the successful fabrication of PDA on the uCNT

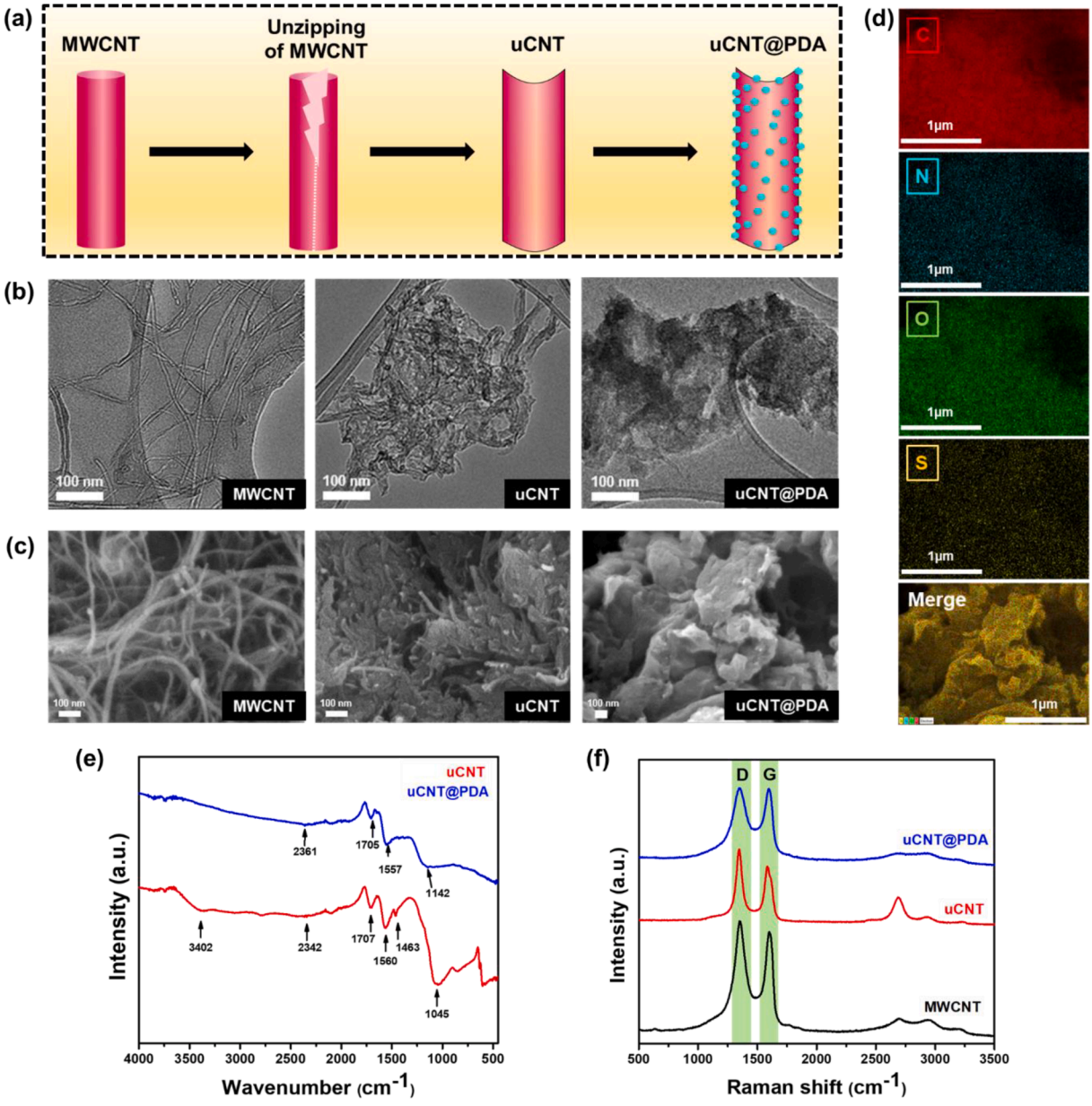

Fig. 1. (a) Scheme of synthesis of uCNT@PDA; (b) TEM and (c) SEM images of MWCNT, uCNT and uCNT@PDA; (d) EDS of uCNT@PDA showing the composition of C, N, O and S; Characterization of uCNT and uCNT@PDA by (e) FT-IR spectra, and (f) Raman spectra.

surface. XPS characterization was further performed for identification of PDA bonding on uCNT surface. In order to confirm the presence of nitrogen, uCNT@PDA were analyzed through XPS survey scan and high resolution spectrum was recorded for C1s, O1s and N1s hybridizations (**Table S2**). C—N bonding in uCNT@PDA was observed through C1s spectra (**Figure S2**) after the deconvolutions. The XPS spectra of C1s showed binding energy peaks at 284.6 eV, 285.8 eV, and 290.3 eV, which have been attributed to the sp^2 or sp^3 carbon (C—C/C═C), C—N amine, and C═O, respectively (**ref**). Additionally, the peak for N1s signals of uCNT@PDA around 400.17 eV (**Figure S2**) was also observed due to the presence of C—N bonding (sp3 hybridization). The resultant peak position has been matched with the published papers (**ref**). Presence of Nitrogen in uCNT@PDA was already confirmed through elemental analysis.

The FTIR and Raman analysis results provided strong evidence for the successful cutting of the MWCNT into the uCNT. According to the FTIR and Raman analyses presented in Fig. 1**(e,f)**, the uCNT were formed after cutting at several positions, which could cause the desired changes in chemical composition. The elemental composition was confirmed through elemental analysis, where the oxygen density was found to be improved, which could undoubtedly indicate the generation of more oxy-functional groups after the unzipping process. The elemental analysis results are provided in **Table S3**. The improved oxygen moieties were responsible for the formation of oxygen radicals and charges, which could enhance the zeta potential. In the FTIR spectrum of the uCNT, vibration bands at 3402 cm^{-1} (–OH), 1707 cm^{-1} (-C═O), and 1045 cm^{-1} (C—O—C) were observed, whereas the vibration bands for the –OH group nearly disappeared in the spectrum of uCNT@PDA. A peak appeared at 1705 cm^{-1} and 1557 cm^{-1} were attributed to the characteristic absorption of the phenyl groups. This clearly indicates the presence of PDA on the uCNT surface, and these PDA structures were bonded with the hydroxyl groups of the uCNT. All representative vibration bands were confirmed and matched well with the reported FTIR peak values. Other representative peaks at 1045 cm^{-1} and 1463 cm^{-1} were assigned to the scissoring of CH_2 and OH of the PDA catechol groups, respectively. These peaks were not easily visible, which may be caused by the weak response of the black material to IR rays [44,45]. The FTIR analysis results provided information to confirm the successful synthesis of the uCNT and uCNT@PDA.

Raman spectroscopy is a very important technique for characterizing carbonaceous materials [46]. The Raman spectra of the MWCNTs, uCNTs, and uCNT@PDA are shown in Fig. 1**(f)**. In this study, two representative peaks in the region between 1000 cm^{-1} and 1700 cm^{-1} were clearly observed. A peak at 1348 cm^{-1} is for the D-band because of disordered boundaries of sp^3 carbon atoms, and a Raman peak around 1598 cm^{-1} is for the G-band, which is because of the Raman-active vibration of sp^2 hybridized carbon atoms from aromatic structures [47]. In general, the intensity ratio of the D- and G-bands can be used to evaluate the extent of carbon-containing defects in adsorbents [48]. The intensity ratios (I_D/IG) of the D- and G-bands were calculated for the MWCNTs, uCNTs, and uCP, and the representative I_D/IG values were 1.08, 1.25, and 1.004, respectively. The I_D/IG ratio of the uCNT was higher than that of the MWCNT because of the chemical and structural modification of the uCNT surface due to the successful unzipping process. Moreover, a 2D peak was observed in the Raman spectra of MWCNT, uCNT, and uCNT@PDA, which was caused by the overtone of the D-band peak at approximately 2670 cm^{-1}. This representative peak is attributed to a double-resonance transition in the carbon material, which is only Raman-active in the presence of defects, that is, surface modification [49]. This representative peak was observed to be highly intense in the Raman spectrum of the uCNT, which is a clear indication of the formation of alien functional groups on the surface, whereas it was much less intense in the Raman spectrum of the MWCNT and uCNT@PDA. The Raman analysis results were analogous to the those of the FTIR results. In addition, a broad and intense D-band band indicated the presence of amorphous material in the sample. These results were consistent with the presence of broad peaks in the XRD pattern. The Raman peaks in each spectrum were very broad and became narrow after unzipping and PDA fabrication. These results were consistent with those of the XRD results (**Figure S3**), where a broad XRD peak for uCNT@PDA and uCNT was clearly observed in the XRD pattern. Hence, this provided evidence for the confirmation of the amorphous nature of the synthesized materials.

The charge information was obtained using zeta potential analysis (**Figure S4**), where the charge on uCNT changed from positively charged MWCNT to highly negative because of the formation of various carboxylic functional groups on the surface. Dopamine is well known for its strong interaction with the sidewalls of CNTs through π–π stacking [50], which is highly beneficial for the spontaneous self-polymerization of dopamine under alkaline conditions. It is important to note that uCNT and uCNT@PDA showed better dispersion in water than MWCNT. Notably, the homogenous dispersion of concentrated PDA on the uCNT surface helps to enhance the desired properties, which are required for further applicability of the material. Based on the characterization results, the syntheses of uCNT and uCNT@PDA were successfully determined.

3.2. Characterization of nanofibers

The uCNT@PDA (0.25, 0.5, and 1%) was added to the PCL solution to fabricate nanofiber mats by electrospinning. The surface morphology was observed using the SEM analysis, and the diameter of the nanofibers was calculated using the algorithm reported by Murphy et al. [51] The results are shown in Fig. 2**(a).** The SIMPoly MATLAB method was used to determine the size of the nanofibers. The surface appearances of the pure PCL and uCNT@PDA-containing PCL nanofibers were almost similar, with the appearance of a slightly rough texture, which is possibly because of the evaporation of the DMF solution during the electrospinning of the nanofiber. The diameter of the pure PCL nanofiber was 32.3 ± 9.4 nm. After incorporation of uCNT@PDA, the diameter of the PCL/uCNT@PDA nanofiber decreased from 47.1 ± 18.9 nm to 32. ± 11.4 nm with increasing concentrations of uCNT@PDA. However, the uniformity of the nanofibers obtained from PCL was observed to be more than that of the hybrid nanofibers.

In addition, the FTIR spectra of the PCL-loaded uCNT@PDA samples (Fig. 2**(b)**) were recorded, and the representative band positions of the PCL material were well-matched with the vibrational bands of PCL in PCL-loaded carbon materials [52]. XRD analysis of the PCL-loaded uCNT@PDA samples was performed, and the XRD patterns were recorded for all the PCL-loaded samples (0.25%–1.0%). Interestingly, the XRD peaks matched the XRD pattern of PCL [53]. In brief, the XRD patterns at 2θ ranging from 5° to 30° for the pure PCL and uCNT@PDA-incorporated nanofibers are presented in Fig. 2**(c)**. Pure PCL exhibited two prominent characteristic peaks at Bragg angles of 2θ = 21.4° and 23.6° owing to the 110 and 200 reflections, respectively. These sharp peaks indicate the crystalline nature of PCL. Furthermore, the crystalline property of the PCL/uCNT@PDA nanofibers was lower than that of the PCL nanofibers; hence, the low intensity of the respective peaks. For PCL/uCNT@PDA-0.25, the intensity of the peaks was the lowest, indicating a reduction in the degree of crystallinity. The reduction in crystallinity indicated an extension of the amorphous regions, and this phenomenon further affected the biodegradability of the pure PCL and its composite films. However, increasing the content of uCNT@PDA increased the crystallinity to some extent, which was reflected in the intensity peaks of PCL/uCNT@PDA-0.5 and PCL/uCNT@PDA-1. This demonstrates that some interactions occurred between PCL and the uCNT@PDA composite.

3.3. Mechanical testing

Mechanical testing was conducted on the films of the PCL, PCL/uCNT@PDA-0.25, PCL/uCNT@PDA-0.5, and PCL/uCNT@PDA-1

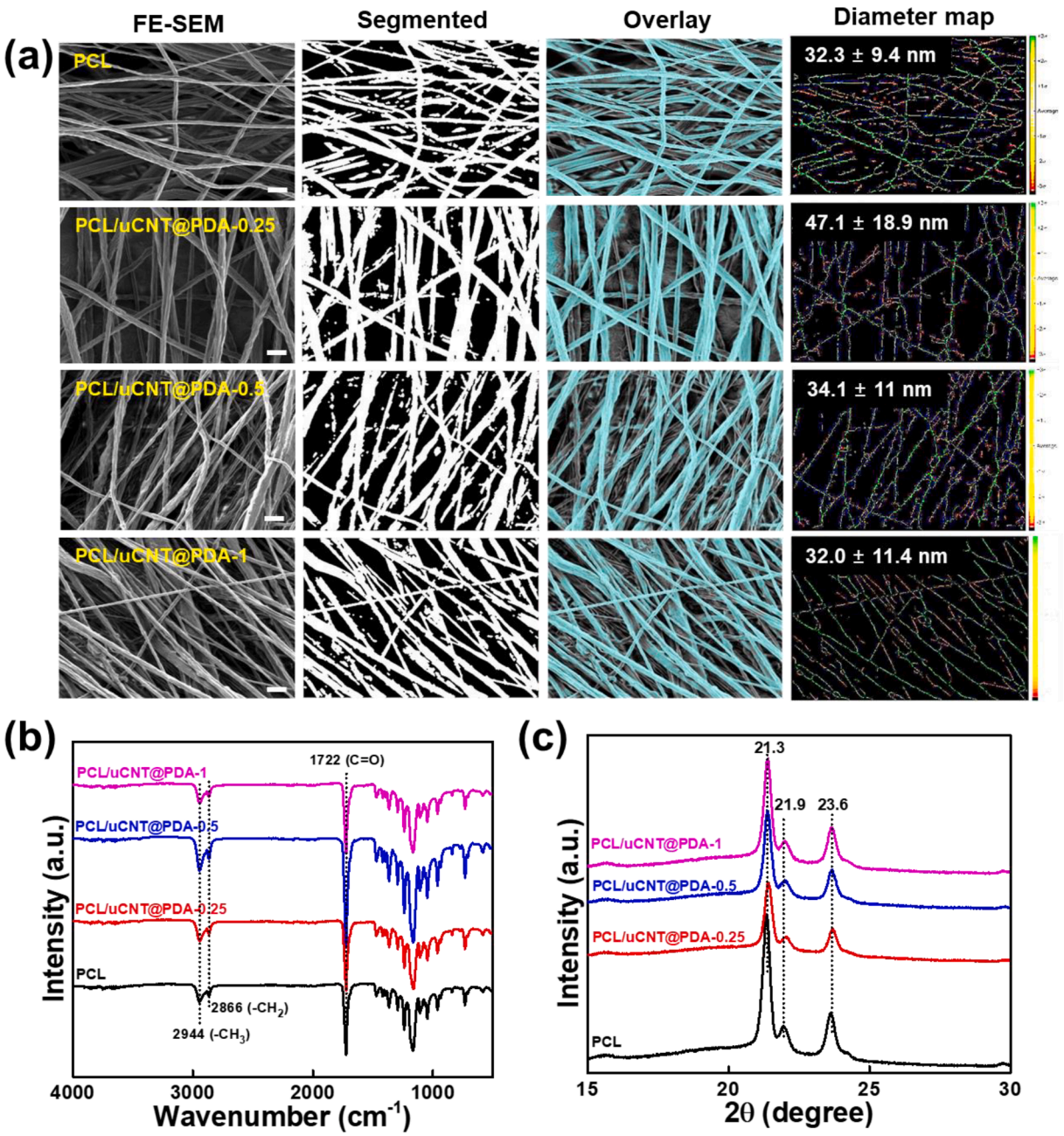

Fig. 2. (a) FE-SEM morphology of PCL and PCL/uCNT@PDA nanofibers with their diameters and their (b) FTIR spectra and (c) XRD patterns.

samples. The dimensions of the fabricated films are given the **Table S4**. The mechanical properties under uniaxial stress are shown in Fig. 3**(a)**. The mechanical properties were influenced by the presence of the uCNT@PDA. PCL/uCNT@PDA-1 showed enhanced elongation at break compared to the pure PCL film. This was because of the possible strong interactions between PCL and uCNT@PDA. A high concentration of uCNT@PDA made PCL tougher. On the other hand, low concentrations can reduce the toughness and mechanical properties of the films. As shown in **Figure S5**, the tensile strength of the PCL/uCNT@PDA-1 film was higher than those of the other samples. Similar results were obtained when PDA and CNT was incorporated in PCL [54,55]. Comparison of mechanical properties of carbon materials with PCL is shown in Table 2**.**

3.4. TGA

TGA was performed to analyze the thermal stability of the PCL/uCNT@PDA composite films. Degradation of PCL was initiated at approximately 230 °C and ended in the range of 400–410 °C. These results are in good agreement with previously reported results [56]. The weight loss of PCL was observed to be 90% at approximately 410 °C. A similar thermal degradation trend was observed for the PCL/uCNT@PDA films loaded with varying concentrations of uCNT@PDA. However, the initiating temperature for all PCL/uCNT@PDA degradations was slightly lower than that of PCL (Fig. 3**(b)**), and this initiating degradation temperature was proportional to PCL. The TGA analysis showed that uCNT@PDA loaded samples were quite stable below 230 °C, which can be beneficial for versatile applications.

The derivative thermogravimetric (DTG) curves of the PCL and PCL/uCNT@PDA films are presented in **Figure S6**. All films had only one

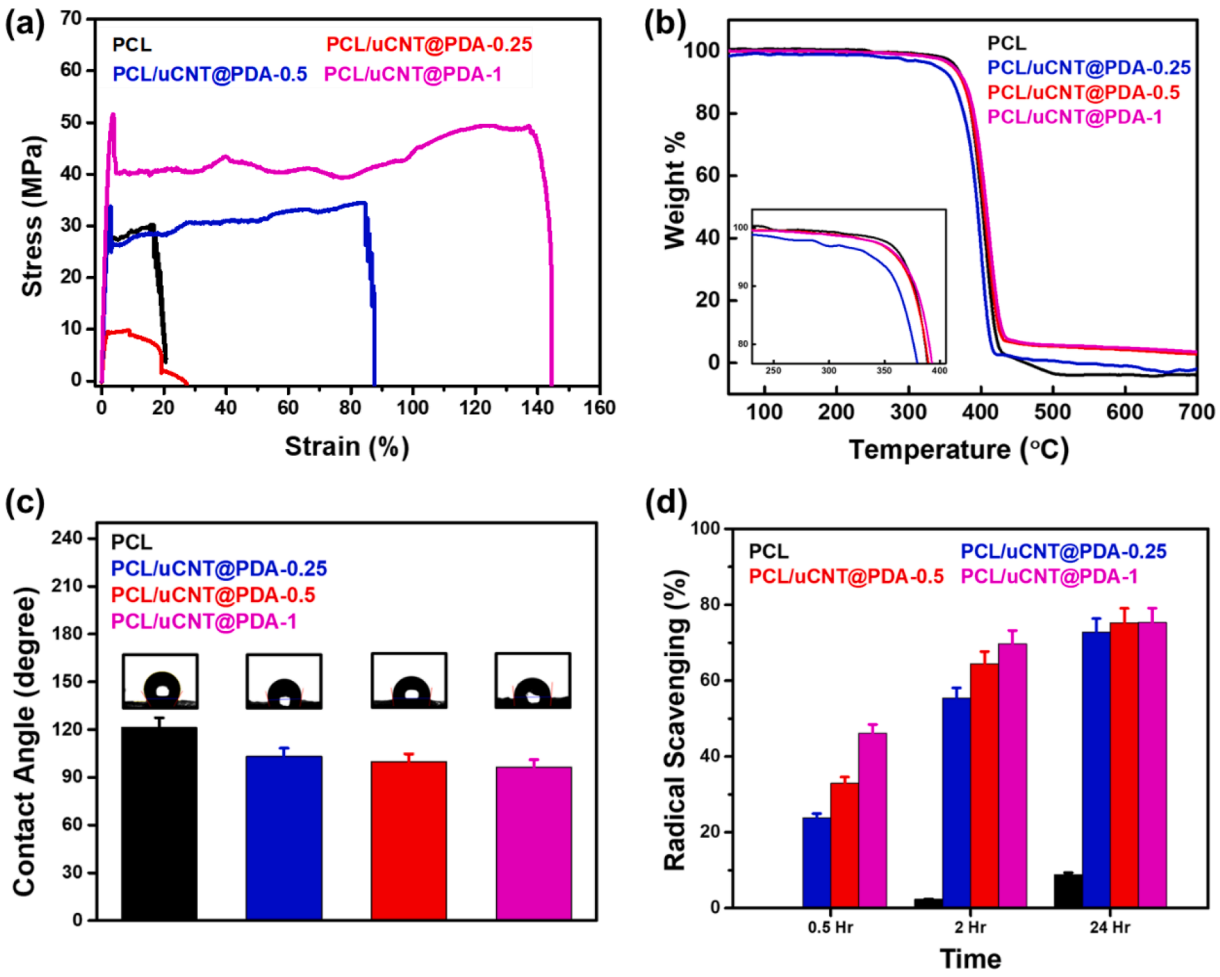

Fig. 3. Mechanical properties of PCL and PCL/uCNT@PDA films: (a) representative stress–strain curves, (b) TGA curves, (c) water contact angle, and (d) DPPH assay.

Table 2
Comparison of mechanical properties, antibacterial effectivity and biocompatibility with different cell lines.

Composite	Elastic modulus (MPa)	Tensile strength (MPa)	Antibacterial efficiency	Biocompatibility	Ref.
PCL	209 ± 21	14.2 ± 1.6	Non-significant	L929 Mouse fibroblast cells	[72,73]
PCL/MWCNT	439 ± 13	18.5 ± 0.5	Non-significant	V79 cells	[55,74]
PCL/PDA	1.9	4.4	Non-significant	MG-63 cells	[54,75,76]
PCL/ graphene	260 ± 26	13.4 ± 0.3	Non-significant	Human adipose-derived stem cells	[77–79]
PCL/Kr/CNT	114	10	–	Mouse fibroblast cell line 3 T3, hAD-MSCs	[80]
PCL/rGO	700	–	27.7%	Rabbit stromal cells	[81,82]
PCL/GO	442 ± 35	27.5 ± 5.7	~30%	Rabbit stromal cells	[72,81,83]
PCL/uCNT@PDA-1	6169.045	19.41 ± 0.18	82%	Human Dermal fibroblast	Present study

Abbreviations: Nanofiber-NF, Keratin-Kr, human adipose-derived Mesenchymal stem cells-hAD-MSCs.

decomposition process with the main peak of PCL at 406 °C. The PCL composite films had lower thermal stability than pure PCL. Specifically, 0.5 and 1% uCNT@PDA incorporated in PCL showed decreased thermal stability than PCL/uCNT@PDA-0.25. The maximum degradation temperature was increased with the increasing content of uCNT@PDA in PCL. Therefore, the results indicated that introduction of uCNT@PDA changes the thermal stability of PCL/uCNT@PDA samples. These observations are in good agreement with the previous studies where CNT and PDA were incorporated separately in PCL [57,58].

3.5. Degradation

The degradation of the PCL-based nanofibers was studied in a buffer solution containing NaOH. As shown in **Figure S7**, the PCL/uCNT@PDA-1 nanofibers exhibited a higher degradation rate than the PCL scaffolds. The PCL/uCNT@PDA nanofibers showed, 40%, and 50% mass loss within 9 days. The degradation rate of PCL scaffolds, such as 3D printed scaffolds and nanofibers, is also very low and takes more than 2 years depending on the molecular weight [59]. Hence, it is expected that the incorporation of uCNT@PDA into the PCL scaffolds will enhance the degradability of overall composite material. Thus, the rate of degradation of the hybrid PCL/uCNT@PDA platforms will increase compared to that of the PCL nanofibers, increasing its application in biodegradable coatings, medical implants and dressing materials.

3.6. Water contact angle

The water contact angle of the PCL/uCNT @PDA nanofibers was determined to understand the wettability of PCL and the influence of uCNT@PDA. The results are shown in Fig. 3**(c)**. PCL is hydrophobic

[60], however, it is biocompatible and widely used in the medical and non-medical field. The pure PCL nanofiber had a contact angle of 121.34°, confirming its hydrophobic surface properties. The incorporation of uCNT@PDA decreased the contact angle by 20–25° and showed lower hydrophobicity than PCL. As shown in Fig. 3**(c),** the contact angle of the nanofibers decreased to 103°, 99°, and 96° with increasing amounts of incorporated uCNT@PDA. However, the overall contact angle was not less than 90°, which represents its hydrophobic property. Therefore, no significant change between PCL and uCNT@PDA loaded samples was observed. This property is highly required for the application of coatings where moisture is not supposed to retain.

3.7. Antioxidant assay

In the 2,2-diphenyl-1-picrylhydrazyl (DPPH) assay, DPPH free radicals can be neutralized by accepting an electron or hydrogen atom, leading to a color change in the solution from purple to yellow [61].

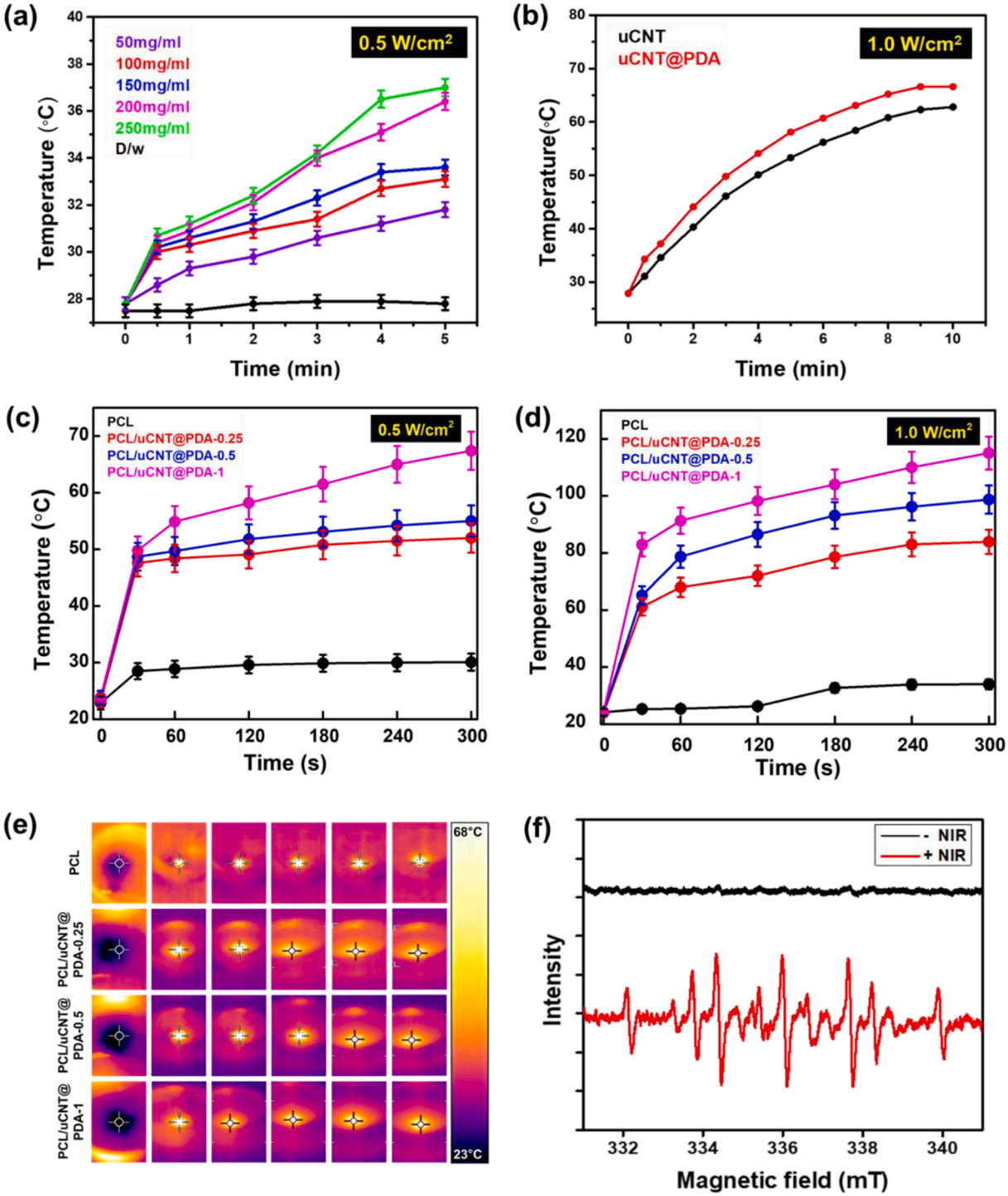

Fig. 4. Photothermal properties **(a)** different concentration of uCNT at 0.5 W/cm^2, **(b)** temperature increase in uCNT and uCNT@PDA at 1.0 w/cm^2 power density, **(c,d,e)** temperature change in nanofibers at **(c)** 0.5 W/cm^2 and **(d)** 1.0 W/cm^2 with **(e)** infrared thermal images on irradiation of 0.5 W/cm^2 and **(f)** ESR spectra of PCL/uCNT@PDA-0.5 nanofiber with and without 808 nm NIR laser light irradiation.

From Fig. 3**(d),** it can be determined that the DPPH-scavenging efficiency of the PCL/uCNT@PDA nanofibers was dependent on the amount of uCNT@PDA. The DPPH-scavenging efficiency was enhanced by increasing the amount of uCNT@PDA. In the initial 30 min, pure PCL exhibited 0.11% ROS-scavenging activity, whereas PCL/uCNT@PDA-0.25, PCL/uCNT@PDA-0.5, and PCL/uCNT@PDA-1 exhibited 23.75%, 32.93, and 46.14% antioxidant activity, respectively, which can be attributed to the inclusion of uCNT@PDA. The percentage of antioxidant activity increased with time, where PCL showed 8.9% ROS scavenging and 72.71%, 75.29%, and 75.34% with increasing amounts of uCNT@PDA content in the nanofibers. It is well known that wound sites could produce excessive ROS, which might result in oxidative stress [62]. Owing to the presence of catechol groups, uCNT@PDA showed excellent antioxidant and free radical scavenging activities [63]. Therefore, PCL/uCNT@PDA-0.5 and PCL/uCNT@PDA-1 nanofiber mats displayed excellent antioxidant ability, which would have great potential as wound dressing materials for wound healing and antibacterial activity.

3.8. Photothermal performance

To evaluate the photothermal conversion ability, the uCNT, uCNT@PDA, and PCL/uCNT@PDA samples were irradiated with NIR light. Fig. 4**(a)** shows the temperature elevation of uCNT of different concentrations upon irradiation with NIR laser light (0.5 W/cm^2). The temperature increased from 27.9 °C to 31.8 °C and 37 °C for 50 μg/ml and 250 μg/ml of uCNT after irradiation with NIR light for 5 min. Similarly, the temperature of 250 μg/ml of uCNT and uCNT@PDA dispersions also increased to 65 °C and 70 °C after irradiation with 1.0 W/cm^2 power density NIR light (Fig. 4 **(b)**). These results imply that the uCNT and uCNT@PDA nanofibers have high photothermal conversion capacities.

The photothermal effect of uCNT@PDA-incorporated PCL nanofibers were also detected using 808 nm NIR light with different power densities (0.5 and 1.0 W/cm^2) for 5 min. The graphs presented in Fig. 4**(c,d,e)** show the increase in the temperature of the nanofibers at varying times of irradiation. The PCL nanofiber, considered a control, exhibited negligible increase in temperature under both 0.5 and 1.0 W/cm^2 power NIR light. In comparison, the PCL/uCNT@PDA-0.25 nanofibers showed a rapid and significant increase in temperature from 24 °C to 52 °C and 83.9 °C after irradiation with 0.5 and 1.0 W/cm^2 power NIR light for 5 min continuously. Similarly, the temperature of PCL/uCNT@PDA-1 composites also increased to 67.4 °C and 115 °C under 0.5 and 1.0 W/cm^2 power NIR light within 5 min. These results demonstrate that the fabricated nanofibers exhibit a photothermal effect and can be used for various applications, including antibacterial and cancer therapy. Table 1 presents the literature on carbon composites with their NIR properties and applications.

3.9. Radical generation

ESR was employed to evaluate the free radical generation of the PCL/uCNT@PDA nanofiber samples with and without NIR light. The ESR spectra of the sample showed strong signals at 3340, 3355, and 3376 G, with g-factor values of 2.0149, 2.0046, and 2.0050, respectively. Interestingly, the sample displayed a more intense signal, as shown in Fig. 4**(f)**. No ESR signals were detected without the NIR-treated nanofibers, suggesting that no free radicals were generated from the nanofibers. However, the ESR signals of the treated sample clearly show the generation of a high free radical concentration.

3.10. NIR irradiation triggered drug release

Curcumin is widely recognized drug for its medicinal properties, including broad-spectrum antibacterial, anti-inflammatory, and antioxidant properties, and for the treatment of wounds. The release profiles of nanofibers were investigated in 2% Tween 20 and PBS mixture solutions. To understand the release of curcumin from PCL/uCNT@PDA nanofibers in the presence of NIR, 3% curcumin was incorporated into the PCL/uCNT@PDA solution during the fabrication process. The amount of drug released from the nanofibers with and without NIR treatment was calculated. The mechanism of light-assisted release from mats was determined by irradiation with NIR light for 5 min before each reading at different time points. Fig. 5**(b)** shows the NIR-triggered curcumin release patterns from the PCL and PCL/uCNT@PDA nanofibers. Curcumin release in the presence of NIR showed little acceleration compared to that without NIR irradiation. It was observed that 80% of the loaded curcumin was discharged from the PCL/uCNT@PDA/Cur nanofibers within 2 weeks. A steady decrease in drug release was observed after 4 days. The burst release was observed in the first 24 h followed by slow release for the next 1 week. In NIR-triggered drug delivery the amount of drug released was approximately 10% higher than that of the drug delivery in the absence of NIR light. The content released in 320 h at pH 7.5 was 76% for regular and 82% for NIR irradiated release.

The mechanism of release of hydrophobic drugs from PCL scaffolds is primarily diffusion [68,69]. The polymer degradation rate and drug-polymer and drug-media interactions significantly influence drug release [70]. The results showed slightly increased curcumin release upon NIR irradiation and a slightly lower release in the absence of an NIR set.

3.11. Antibacterial assay

To evaluate antibacterial performances by a single NIR light irradiation to nanofibers, bacterial survival experiments against *B. subtilis* and *E. coli* were carried. The platforms were irradiated with the 808 nm laser (0.5 W/cm^2, 10 min) light and bacteria colony were counted using a standard surface plating method. As shown in Fig. 6**(a,b)**, the PCL/uCNT@PDA nanofiber mat showed a bactericidal effect against *B. subtilis* and *E. coli* when irradiated with 808 nm NIR light. For the PCL nanofiber, no bactericidal effect was observed, with or without the NIR treatment. The bacteria killing activity of PCL/uCNT@PDA-0.25, 0.5, and 1 increased up to 24%, 35%, and 44% against *B. subtilis* (Fig. 6**(a)**) and 63%, 68%, and 82% against *E. coli* (Fig. 6**(b)**) in the presence of NIR light, respectively. It is clearly observed that antibacterial activity was enhanced by increasing the amount of uCNT@PDA. The generation of heat and ROS in bacterial cultures is a possible reason for the bactericidal effect of this material. To further visualize the antibacterial property of this mat, the morphology of the membrane integrity of the bacteria treated with NIR on all samples was observed using SEM analysis. As shown in Fig. 7**,** after the NIR treatment on bacteria in PBS and PCL nanofibers, the bacterial membrane was intact without any leakage or rupture. In contrast, the PCL/uCNT@PDA-0.25, PCL/uCNT@PDA-0.5, and PCL/uCNT@PDA-1 platforms showed bacterial shrinkage and rupture of membrane.

In some cases, the cell contents of the bacteria were released, leaving the outer membrane hollow. This confirmed the killing of bacteria. The bactericidal effect on *B. subtilis* was more intense than that on *E. coli*. However, approximately all the bacteria shrank, which is the initial stage of cell damage. Among all the nanofiber membranes, PCL/uCNT@PDA-1 exhibited the best bactericidal efficacy. The photothermal property of uCNT@PDA has a photothermal effect on bacteria, which can change the permeability of the bacterial membrane and denature enzymes and other proteins. The ROS produced by uCNT@PDA can also increase the permeability and thermal sensitivity of damaged bacterial membranes. These two therapies complemented each other and achieved synergistic bactericidal effects. Antibacterial evaluation at high temperature and ROS production because of NIR irradiation on nanofibers confirm this conclusion. Antibacterial properties of different carbon materials have been compared in Table 2**.**

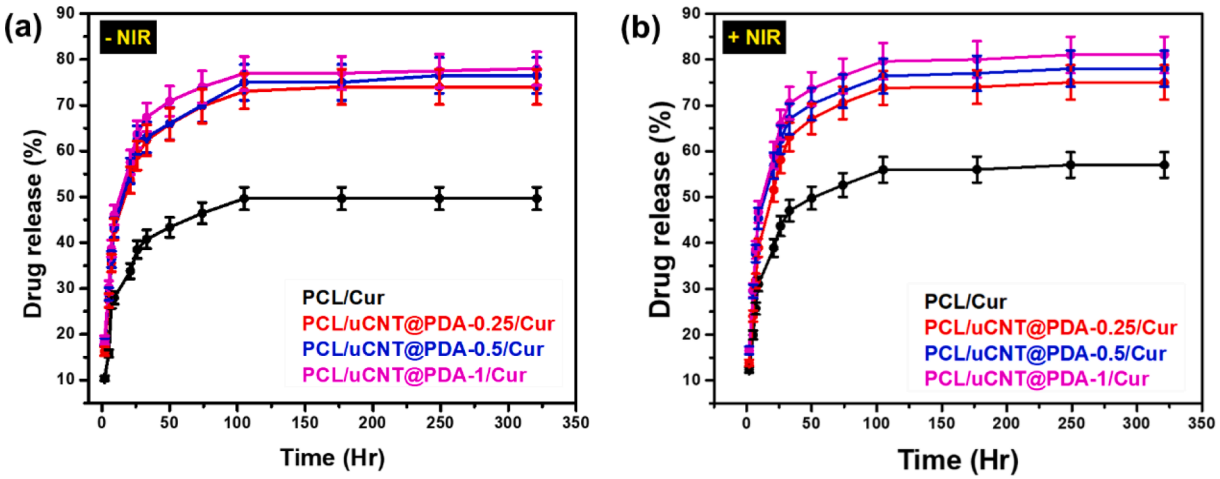

Fig. 5. Behavior of curcumin release in (a) absence of NIR light and (b) presence of NIR light.

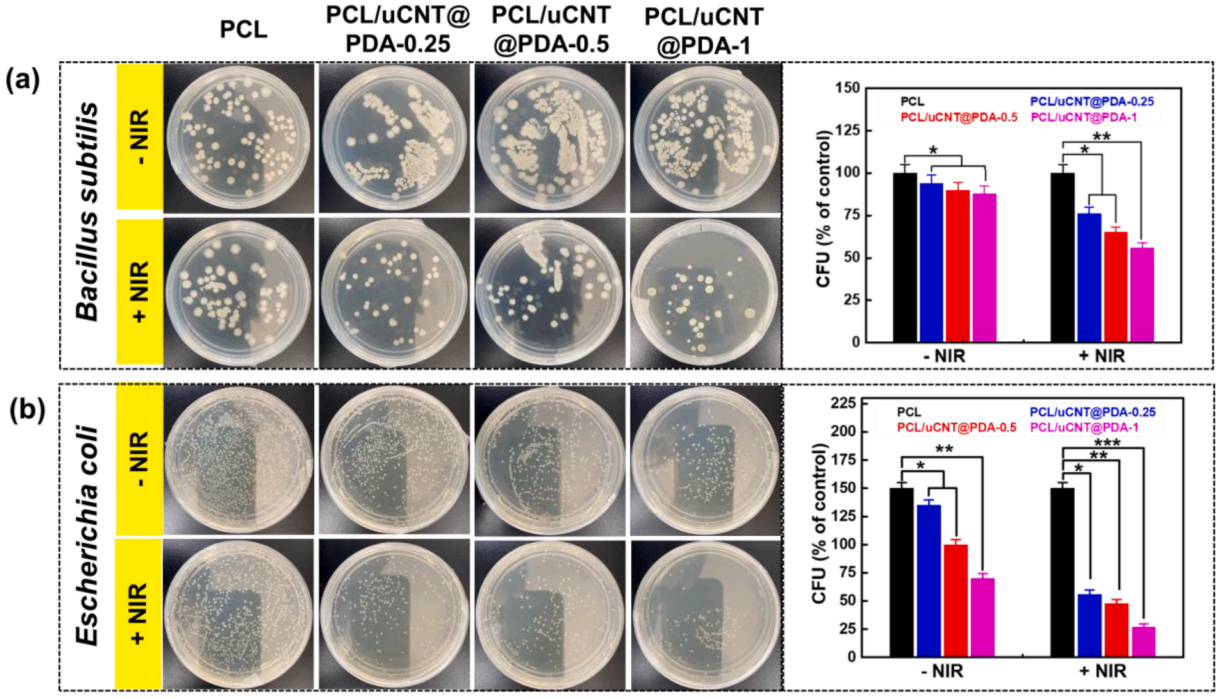

Fig. 6. NIR responsive antibacterial property of the fabricated nanofibers. Antibacterial efficacy of various nanofibers after irradiation with 0.5 W/cm^2 laser light (808 nm) against (a) *Bacillus* sp. and *(b) E.coli* after 24 h culture and colony forming unit (cfu) after 24 h of culture. Data are mean ± SD of triplicated experiments, statistical significance at ***$p < 0.001$.

3.12. Antibiofilm activity

The biofilm degradation property of the PCL/uCNT@PDA nanofibers with and without the NIR treatment was examined. The results presented in Fig. 8 show that the NIR treatment on the biofilm-developed nanofibers disrupted the biofilms when compared to that of the nanofibers without the NIR treatment. After staining the biofilms with crystal violet, it was observed that the NIR-treated wells contained very few bacteria; hence, the stain retained within the wells was comparatively lower than the control set. The results suggest that the NIR treatment of the PCL/uCNT@PDA nanofibers exhibited significant antibiofilm activity.

An increase in the concentration of uCNT@PDA positively affected the biofilm degradation performance of the nanofibers. Therefore, the highest antibiofilm activity was observed for the PCL/uCNT@PDA-1 nanofibers. The biofilms of *B. subtilis* and *E. coli* were disrupted by 40% and 50%, respectively, because of the NIR treatment of PCL/uCNT@PDA-1 nanofibers. In comparison, the antibiofilm activities of control samples were 1% for *B. subtilis* and 4% for *E. coli*. The biofilm degradation by PCL/uCNT@PDA-0.25 was the least as a percentage decrease of only 25% and 19% upon NIR treatment. Suitable antibacterial activities were obtained when α-Fe_2O_3@Au/PDA nanoparticles were treated with NIR light but with a high power density (2.0 W/ cm^2) [71]. Therefore, the developed NIR-responsive platform is a promising approach for degrading biofilms that develop on various surfaces. As a result, PCL/uCNT@PDA nanofibers can easily degrade and inhibit biofilm formation when irradiated with NIR light.

3.13. Cytotoxicity and Live/Dead assay

Cell viability was assessed to check for any adverse effects of the PCL/uCNT@PDA nanofibers on the HDF cells using the WST-8 assay for

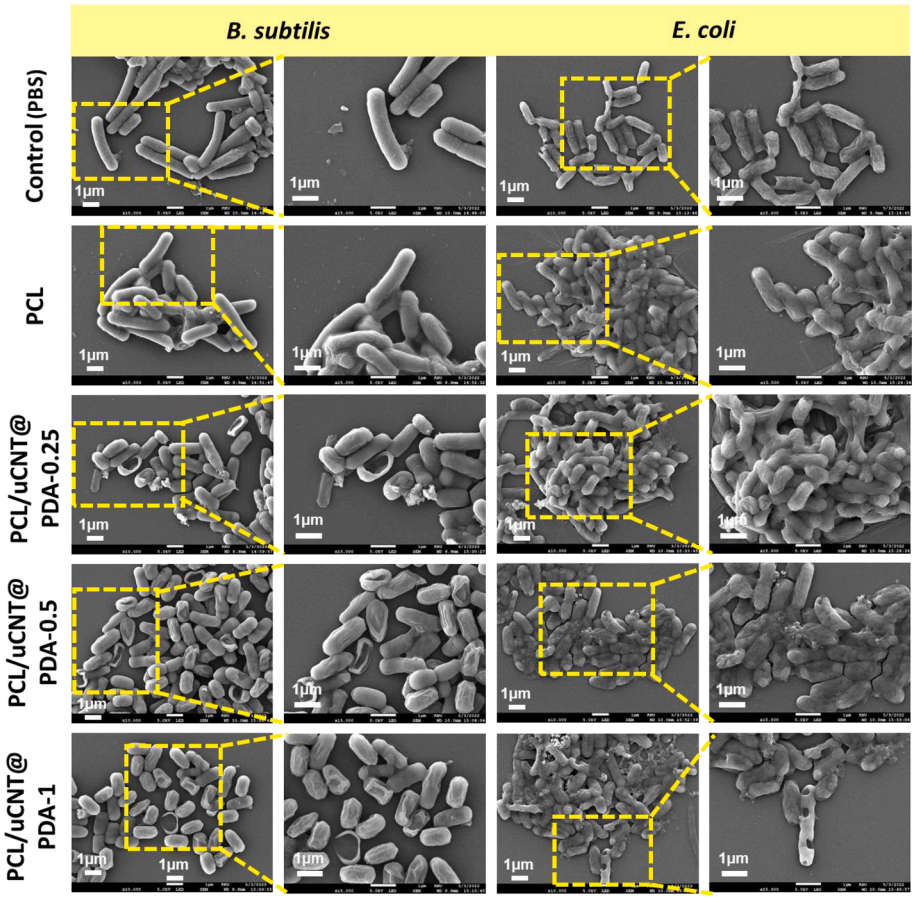

Fig. 7. SEM images of killing of *B. subtilis* and *E.coli* after treatment of 0.5 W/cm^2 laser light (808 nm) NIR irradiation on PCL/uCNT@PDA nanofibers.

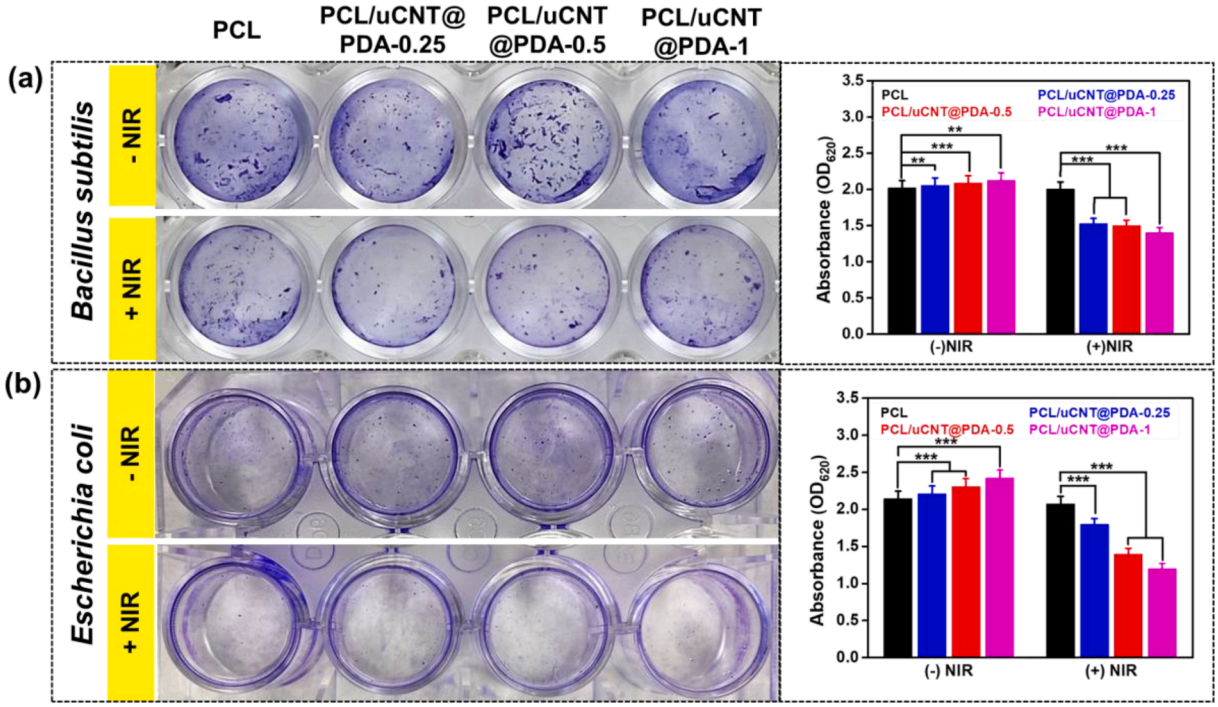

Fig. 8. NIR responsive antibacterial biofilm property of the fabricated nanofibers. Biofilm degradation efficacy of various nanofibers after irradiation with 0.5 W/cm^2 laser light (808 nm) against (a) *Bacillus* sp. And (b) *E. coli* and their respective OD values. Data are mean ± SD of triplicated experiments, statistical significance at $^{**}p < 0.01$, $^{***}p < 0.001$.

1, 3, and 5 days, and the results are presented in Fig. 9**(a)**. Even though the PCL/uCNT@PDA-1 and PCL/uCNT@PDA-0.5 samples showed a decrease in cell viability compared to the PCL samples, a consistent increase in cell proliferation on their individual surfaces was observed. Considering PCL as a control, PCL/uCNT@PDA-0.5, and PCL/uCNT@PDA-1 showed satisfactory biocompatibility with and viability of the HDF cells. It was observed that PCL/uCNT@PDA-0.5 and PCL/uCNT@PDA-1 were less compatible than PCL/uCNT@PDA-0.25 for cell growth. After day 3, the rate of proliferation increased in the uCNT@PDA-incorporated samples.

For Live/Dead images at 3 and 6 days, cultured cells on nanofibers were stained with acridine orange and ethidium bromide staining solution. The Live/Dead assay of HDF with the nanofibers on days 3 and 6 is shown in Fig. 9**(b)**. The images demonstrate that almost all the cells seeded on the nanofiber were live (green). Even on day 6, the cells were viable on the nanofibers, indicating that the fabricated PCL/uCNT@PDA nanofibers were biocompatible and had no toxic effects on HDF cells. Furthermore, the cultured HDF cell morphology resembled a spindle-shaped morphology, indicating that the cells were healthy and followed and spread in the direction of the nanofibers. Thus, the result states that PCL/uCNT@PDA platforms are not hazardous and can be applied in medical sectors for implant coatings and prevent or eradication of bacteria infections. Cytocompatibility of various PCL/carbon materials are listed in Table 2 which shows that carbon materials incorporated in PCL are non-toxic to different cell lines.

4. Conclusion

This study successfully synthesized unzipped CNTs using an eco-friendly-one-pot approach. The prepared uCNTs were modified with mussel-inspired PDA and incorporated into biocompatible PCL to develop the PCL/uCNT@PDA nanofibers. The PCL/uCNT@PDA platforms exhibited excellent photothermal properties at a low power density in a minimum time period (5 min). In addition, the nanofibers showed ROS-scavenging activity in the absence of NIR and the generation of free radicals in the presence of NIR light. An enhanced antibacterial effect against gram-positive and gram-negative bacteria was observed upon NIR laser irradiation. Furthermore, it was found that untreated PCL/uCNT@PDA nanofibers were less effective against the antibiofilm activity. However, when the nanofibers were irradiated with NIR light, the antibiofilm properties were significantly enhanced. Heat was produced by the nanofibers upon NIR light irradiation. The increased temperature killed the bacteria and degraded the bacterial biofilm. The highest antibacterial activity was observed for PCL/uCNT@PDA nanofibers. Curcumin release from the PCL/uCNT@PDA nanofibers showed similar release properties in the presence and absence of NIR light. Moreover, the cell viability of the nanofiber showed no remarkable cytotoxicity. Based on these results, the developed hybrid platforms had potential versatile application in coatings, medical implants, sterilization of water, and removal of bacteria from various surfaces.

Data availability

Data will be made available on request.

CRediT authorship contribution statement

Tejal V. Patil: Conceptualization, Methodology, Data curation. **Sayan Deb Dutta:** Formal analysis, Visualization. **Dinesh K. Patel:** Formal analysis, Visualization. **Keya Ganguly:** Visualization. **Ki-Taek Lim:** Funding acquisition, Project administration.

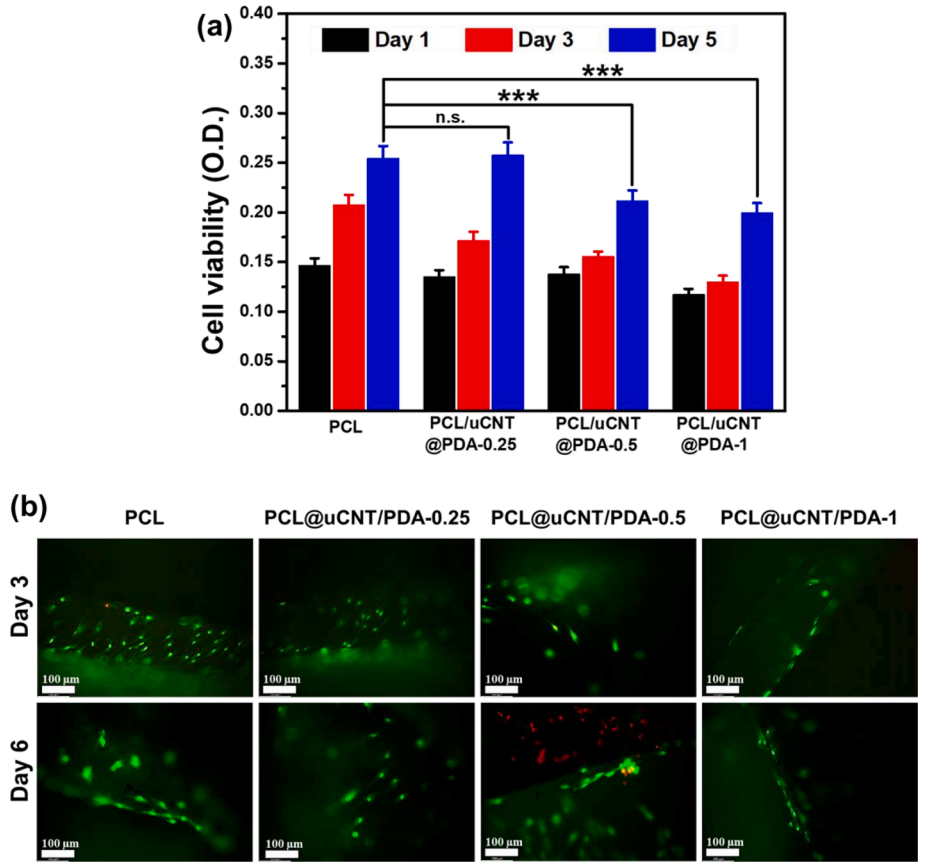

Fig. 9. (a) Cell viability of HDFs in presence of fabricated nanofibers evaluated from WST assay for day 1, 3 and 5, **(b)** Live/dead assay of PCL and PCL/uCNT@PDA nanofibers after incubation of 3 and 6 days. Data are mean ± SD of triplicated experiments, statistical significance at ***$p < 0.001$, n.s.-not significant.

Declaration of Competing Interest

The authors declare that they have no known competing financial interests or personal relationships that could have appeared to influence the work reported in this paper.

Data availability

Data will be made available on request.

Acknowledgments

This work is financially supported by the Basic Research Program through the National Research Foundation of Korea (NRF) funded by the Ministry of Education (Grant No. NRF-2018R1A6A1A03025582, NRF-2019R1D1A3A03103828, and NRF 2022R1I1A3063302).

Appendix A. Supplementary data

Supplementary data to this article can be found online at https://doi.org/10.1016/j.apsusc.2022.155949.

References

[1] S. Doron, S.L. Gorbach, Bacterial Infections: Overview, International Encyclopedia of, Public Health (2008) 273–282.
[2] W.-N. Wang, P. Pei, Z.-Y. Chu, B.-J. Chen, H.-S. Qian, Z.-B. Zha, W. Zhou, T. Liu, M. Shao, H. Wang, Bi2S3 coated Au nanorods for enhanced photodynamic and photothermal antibacterial activities under NIR light, Chem. Eng. J. 397 (2020), 125488.
[3] S. Yu, G. Li, P. Zhao, Q. Cheng, Q. He, D. Ma, W. Xue, NIR-Laser-Controlled Hydrogen-Releasing PdH Nanohydride for Synergistic Hydrogen-Photothermal Antibacterial and Wound-Healing Therapies, Adv. Funct. Mater. 29 (2019) 1905697.
[4] Z. Yuan, B. Tao, Y. He, J. Liu, C. Lin, X. Shen, Y. Ding, Y. Yu, C. Mu, P. Liu, K. Cai, Biocompatible MoS2/PDA-RGD coating on titanium implant with antibacterial property via intrinsic ROS-independent oxidative stress and NIR irradiation, Biomaterials 217 (2019), 119290.
[5] S. Huang, S. Xu, Y. Hu, X. Zhao, L. Chang, Z. Chen, X. Mei, Preparation of NIR-responsive, ROS-generating and antibacterial black phosphorus quantum dots for promoting the MRSA-infected wound healing in diabetic rats, Acta Biomater. 137 (2022) 199–217.
[6] J. Shan, K. Yang, W. Xiu, Q. Qiu, S. Dai, L. Yuwen, L. Weng, Z. Teng, L. Wang, Cu2MoS4 Nanozyme with NIR-II Light Enhanced Catalytic Activity for Efficient Eradication of Multidrug-Resistant Bacteria, Small 16 (2020) 2001099.
[7] D.Y. Gao, X. Ji, J.L. Wang, Y.T. Wang, D.L. Li, Y.B. Liu, K.W. Chang, J.L. Qu, J. Zheng, Z. Yuan, Engineering a protein-based nanoplatform as an antibacterial agent for light activated dual-modal photothermal and photodynamic therapy of infection in both the NIR I and II windows, J. Mater. Chem. B 6 (2018) 732–739.
[8] Y. Zou, Y. Zhang, Q. Yu, H. Chen, Photothermal bactericidal surfaces: killing bacteria using light instead of biocides, Biomaterials, Science 9 (2021) 10–22.
[9] C. Liu, M. Zhang, H. Geng, P. Zhang, Z. Zheng, Y. Zhou, W. He, NIR enhanced peroxidase-like activity of Au@CeO2 hybrid nanozyme by plasmon-induced hot electrons and photothermal effect for bacteria killing, Appl. Catal. B 295 (2021), 120317.
[10] D. Han, Y. Han, J. Li, X. Liu, K.W.K. Yeung, Y. Zheng, Z. Cui, X. Yang, Y. Liang, Z. Li, S. Zhu, X. Yuan, X. Feng, C. Yang, S. Wu, Enhanced photocatalytic activity and photothermal effects of cu-doped metal-organic frameworks for rapid treatment of bacteria-infected wounds, Appl. Catal. B 261 (2020), 118248.
[11] J. Cao, B. Zhu, K. Zheng, S. He, L. Meng, J. Song, H. Yang, Recent Progress in NIR-II Contrast Agent for Biological Imaging, Front. Bioeng. Biotechnol. 7 (2020).
[12] W. He, H.-K. Kim, W.G. Wamer, D. Melka, J.H. Callahan, J.-J. Yin, Photogenerated Charge Carriers and Reactive Oxygen Species in ZnO/Au Hybrid Nanostructures with Enhanced Photocatalytic and Antibacterial Activity, J. Am. Chem. Soc. 136 (2014) 750–757.
[13] J. Lin, Z. He, F. Liu, J. Feng, C. Huang, X. Sun, H. Deng, Hybrid hydrogels for synergistic periodontal antibacterial treatment with sustained drug release and NIR-responsive photothermal effect, Int. J. Nanomed. 15 (2020) 5377.
[14] W. Cao, L. Yue, I.M. Khan, Z. Wang, Polyethylenimine modified MoS2 nanocomposite with high stability and enhanced photothermal antibacterial activity, J. Photochem. Photobiol. A Chem. 401 (2020), 112762.
[15] X. Ding, P. Yuan, N. Gao, H. Zhu, Y.Y. Yang, Q.-H. Xu, Au-Ag core-shell nanoparticles for simultaneous bacterial imaging and synergistic antibacterial activity, Nanomedicine: Nanotechnology, Biol. Med. 13 (2017) 297–305.
[16] C. Mutalik, Y.-C. Hsiao, Y.-H. Chang, D.I. Krisnawati, M. Alimansur, A. Jazidie, M. Nuh, C.-C. Chang, D.-Y. Wang, T.-R. Kuo, High UV-Vis-NIR Light-Induced Antibacterial Activity by Heterostructured TiO(2)-FeS(2) Nanocomposites, Int. J. Nanomed. 15 (2020) 8911–8920.
[17] R. Dubey, D. Dutta, A. Sarkar, P. Chattopadhyay, Functionalized carbon nanotubes: synthesis, properties and applications in water purification, drug delivery, and material and biomedical sciences, Nanoscale Adv. 3 (2021) 5722–5744.
[18] A. Dey, O.P. Bajpai, A.K. Sikder, S. Chattopadhyay, M.A. Shafeeuulla Khan, Recent advances in CNT/graphene based thermoelectric polymer nanocomposite: A proficient move towards waste energy harvesting, Renew. Sustain. Energy Rev. 53 (2016) 653–671.
[19] K.K. Singh, A. Singh, S. Rai, A study on nanomaterials for water purification, Mater. Today:. Proc. 51 (2022) 1157–1163.
[20] D.K. Patel, S.D. Dutta, K. Ganguly, J.-W. Kim, K.-T. Lim, Enhanced osteogenic potential of unzipped carbon nanotubes for tissue engineering, J. Biomed. Mater. Res. A 109 (2021) 1869–1880.
[21] T.V. Patil, D.K. Patel, S.D. Dutta, K. Ganguly, A. Randhawa, K.-T. Lim, Carbon Nanotubes-Based Hydrogels for Bacterial Eradiation and Wound-Healing Applications, Appl. Sci. 11 (2021) 9550.
[22] M. Sheikhpour, H. Jannati, S.D. Siadat, P. Safarian, Antimicrobial activity and drug delivery ability of Functionalized Multi-Walled Carbon Nanotubes Nanofluid on staphylococcus aureus, Nanomed. Res. J. 6 (2021) 248–256.
[23] S. Agarwal, N.E. Kallmyer, D.X. Vang, A.V. Ramirez, M.M. Islam, A.C. Hillier, L. J. Halverson, N.F. Reuel, Single-Walled Carbon Nanotube Probes for the Characterization of Biofilm-Degrading Enzymes Demonstrated against Pseudomonas aeruginosa Extracellular Matrices, Anal. Chem. 94 (2022) 856–865.
[24] S. Mondal, S. Ghosh, C.R. Raj, Unzipping of Single-Walled Carbon Nanotube for the Development of Electrocatalytically Active Hybrid Catalyst of Graphitic Carbon and Pd Nanoparticles, ACS Omega 3 (2018) 622–630.
[25] A. Vashist, A. Kaushik, A. Vashist, V. Sagar, A. Ghosal, Y.K. Gupta, S. Ahmad, M. Nair, Advances in Carbon Nanotubes-Hydrogel Hybrids in Nanomedicine for Therapeutics, Adv. Healthc. Mater. 7 (2018) 1701213.
[26] T.L. Nguyen, M. Takai, K. Ishihara, K. Oyama, S. Fujii, S.-I. Yusa, Facile preparation of water-soluble multiwalled carbon nanotubes bearing phosphorylcholine groups for heat generation under near-infrared irradiation, Polym. J. 53 (2021) 1001–1009.
[27] Y. Liang, X. Zhao, T. Hu, Y. Han, B. Guo, Mussel-inspired, antibacterial, conductive, antioxidant, injectable composite hydrogel wound dressing to promote the regeneration of infected skin, J. Colloid Interface Sci. 556 (2019) 514–528.
[28] Y.H. Ding, M. Floren, W. Tan, Mussel-inspired polydopamine for bio-surface functionalization, Biosurf. Biotribol. 2 (2016) 121–136.
[29] Z. Li, X. Zhang, S. Wang, Y. Yang, B. Qin, K. Wang, T. Xie, Y. Wei, Y. Ji, Polydopamine coated shape memory polymer: enabling light triggered shape recovery, light controlled shape reprogramming and surface functionalization, Chem. Sci. 7 (2016) 4741–4747.
[30] H. Lv, H. Chi, X. Yang, J. Peng, W. Wang, D. Tang, Polydopamine-assisted shape memory of polyurethane nanofibers with light-induced tunable responsiveness and improved cell adhesiveness, Colloids Surf. A Physicochem. Eng. Asp. 627 (2021), 127100.
[31] J. Hu, L. Yang, P. Yang, S. Jiang, X. Liu, Y. Li, Polydopamine free radical scavengers, Biomaterials, Science 8 (2020) 4940–4950.
[32] H. Yuan, T. Li, Y. Wang, P. Ma, M. Du, T. Liu, Y. Yan, H. Bai, M. Chen, W. Dong, Photoprotective and multifunctional polymer film with excellent near-infrared and UV shielding properties, Compos. Commun. 22 (2020), 100443.
[33] I. Altinbasak, R. Jijie, A. Barras, B. Golba, R. Sanyal, J. Bouckaert, D. Drider, R. Bilyy, T. Dumych, S. Paryzhak, V. Vovk, R. Boukherroub, A. Sanyal, S. Szunerits, Reduced Graphene-Oxide-Embedded Polymeric Nanofiber Mats: An "On-Demand" Photothermally Triggered Antibiotic Release Platform, ACS Appl. Mater. Interfaces 10 (2018) 41098–41106.
[34] Y.S. Lui, W.T. Sow, L.P. Tan, Y. Wu, Y. Lai, H. Li, 4D printing and stimuli-responsive materials in biomedical aspects, Acta Biomater. 92 (2019) 19–36.
[35] P. Lavrador, M.R. Esteves, V.M. Gaspar, J.F. Mano, Stimuli-Responsive Nanocomposite Hydrogels for Biomedical Applications, Adv. Funct. Mater. 31 (2021) 2005941.
[36] R. Tabanelli, S. Brogi, V. Calderone, Improving Curcumin Bioavailability: Current Strategies and Future Perspectives, Pharmaceutics 13 (2021) 1715.
[37] C. Wang, Y.-S. Li, J. Jiang, W.-H. Chiang, Controllable Tailoring Graphene Nanoribbons with Tunable Surface Functionalities: An Effective Strategy toward High-Performance Lithium-Ion Batteries, ACS Appl. Mater. Interfaces 7 (2015) 17441–17449.
[38] D.V. Kosynkin, A.L. Higginbotham, A. Sinitskii, J.R. Lomeda, A. Dimiev, B.K. Price, J.M. Tour, Longitudinal unzipping of carbon nanotubes to form graphene nanoribbons, Nature 458 (2009) 872–876.
[39] N.L. Rangel, J.C. Sotelo, J.M. Seminario, Mechanism of carbon nanotubes unzipping into graphene ribbons, J. Chem. Phys. 131 (2009), 031105.
[40] Q. Wan, J. Tian, M. Liu, G. Zeng, Q. Huang, K. Wang, Q. Zhang, F. Deng, X. Zhang, Y. Wei, Surface modification of carbon nanotubes via combination of mussel inspired chemistry and chain transfer free radical polymerization, Appl. Surf. Sci. 346 (2015) 335–341.
[41] R. Gharibi, H. Yeganeh, A. Rezapour-Lactoee, Z.M. Hassan, Stimulation of Wound Healing by Electroactive, Antibacterial, and Antioxidant Polyurethane/Siloxane Dressing Membranes: In Vitro and in Vivo Evaluations, ACS Appl. Mater. Interfaces 7 (2015) 24296–24311.
[42] J. Sun, L. Song, Y. Fan, L. Tian, S. Luan, S. Niu, L. Ren, W. Ming, J. Zhao, Synergistic Photodynamic and Photothermal Antibacterial Nanocomposite Membrane Triggered by Single NIR Light Source, ACS Appl. Mater. Interfaces 11 (2019) 26581–26589.
[43] M. Moazzen, A. Mousavi Khaneghah, N. Shariatifar, M. Ahmadloo, I. Eş, A. N. Baghani, S. Yousefinejad, M. Alimohammadi, A. Azari, S. Dobaradaran, N. Rastkari, S. Nazmara, M. Delikhoon, G. Jahed Khaniki, Multi-walled carbon

nanotubes modified with iron oxide and silver nanoparticles (MWCNT-Fe3O4/Ag) as a novel adsorbent for determining PAEs in carbonated soft drinks using magnetic SPE-GC/MS method, Arab. J. Chem. 12 (2019) 476–488.
[44] N. Rahoui, M. Hegazy, B. Jiang, N. Taloub, Y.D. Huang, Particles size estimation of polydopamine based polymeric nanoparticles using near-infrared spectroscopy combined with linear regression method, Am. J. Anal. Chem. 9 (2018) 273.
[45] J. Luo, N. Zhang, R. Liu, X. Liu, In situ green synthesis of Au nanoparticles onto polydopamine-functionalized graphene for catalytic reduction of nitrophenol, RSC Adv. 4 (2014) 64816–64824.
[46] P.P. Upare, J.-W. Yoon, M.Y. Kim, H.-Y. Kang, D.W. Hwang, Y.K. Hwang, H. H. Kung, J.-S. Chang, Chemical conversion of biomass-derived hexose sugars to levulinic acid over sulfonic acid-functionalized graphene oxide catalysts, Green Chem. 15 (2013) 2935–2943.
[47] A.C. Ferrari, J.C. Meyer, V. Scardaci, C. Casiraghi, M. Lazzeri, F. Mauri, S. Piscanec, D. Jiang, K.S. Novoselov, S. Roth, A.K. Geim, Raman Spectrum of Graphene and Graphene Layers, Phys. Rev. Lett. 97 (2006), 187401.
[48] D.B. Schuepfer, F. Badaczewski, J.M. Guerra-Castro, D.M. Hofmann, C. Heiliger, B. Smarsly, P.J. Klar, Assessing the structural properties of graphitic and non-graphitic carbons by Raman spectroscopy, Carbon 161 (2020) 359–372.
[49] A. Jorio, R. Saito, Raman spectroscopy for carbon nanotube applications, J. Appl. Phys. 129 (2021), 021102.
[50] Y. Zhou, Y. Fang, R.P. Ramasamy, Non-Covalent Functionalization of Carbon Nanotubes for Electrochemical Biosensor Development, Sensors (Basel) 19 (2019) 392.
[51] R. Murphy, A. Turcott, L. Banuelos, E. Dowey, B. Goodwin, K.O.H. Cardinal, SIMPoly: A Matlab-Based Image Analysis Tool to Measure Electrospun Polymer Scaffold Fiber Diameter, Tissue Eng. Part C Methods 26 (2020) 628–636.
[52] I. Castilla-Cortázar, A. Vidaurre, B. Marí, A.J. Campillo-Fernández, Morphology, Crystallinity, and Molecular Weight of Poly(ε-caprolactone)/Graphene Oxide Hybrids, Polymers 11 (2019) 1099.
[53] R. Balu, T.S.S. Kumar, M. Ramalingam, S. Ramakrishna, Electrospun Polycaprolactone/Poly(1,4-butylene adipate-co-polycaprolactam) Blends: Potential Biodegradable Scaffold for Bone Tissue Regeneration, J. Biomater. Tissue Eng. 1 (2011) 30–39.
[54] M.M. Hasani-Sadrabadi, P. Sarrion, N. Nakatsuka, T.D. Young, N. Taghdiri, S. Ansari, T. Aghaloo, S. Li, A. Khademhosseini, P.S. Weiss, A. Moshaverinia, Hierarchically Patterned Polydopamine-Containing Membranes for Periodontal Tissue Engineering, ACS Nano 13 (2019) 3830–3838.
[55] S. Kumar, S. Bose, K. Chatterjee, Amine-functionalized multiwall carbon nanotubes impart osteoinductive and bactericidal properties in poly(ε-caprolactone) composites, RSC Adv. 4 (2014) 19086–19098.
[56] K.J. Figueroa-Lopez, J.L. Castro-Mayorga, M.M. Andrade-Mahecha, L. Cabedo, J. M. Lagaron, Antibacterial and Barrier Properties of Gelatin Coated by Electrospun Polycaprolactone Ultrathin Fibers Containing Black Pepper Oleoresin of Interest in Active Food Biopackaging Applications, Nanomaterials 8 (2018) 199.
[57] Z. Terzopoulou, D.N. Bikiaris, K.S. Triantafyllidis, G. Potsi, D. Gournis, G. Z. Papageorgiou, P. Rudolf, Mechanical, thermal and decomposition behavior of poly(ε-caprolactone) nanocomposites with clay-supported carbon nanotube hybrids, Thermochim. Acta 642 (2016) 67–80.
[58] S. Zuppolini, I. Cruz-Maya, V. Guarino, A. Borriello, Optimization of Polydopamine Coatings onto Poly–ε–Caprolactone Electrospun Fibers for the Fabrication of Bio-Electroconductive Interfaces, J. Funct. Biomater. 11 (2020) 19.
[59] H. Sun, L. Mei, C. Song, X. Cui, P. Wang, The in vivo degradation, absorption and excretion of PCL-based implant, Biomaterials 27 (2006) 1735–1740.
[60] C. Gao, J. Jiang, J. Wang, Y. Wang, Y. Zhang, C. Rao, Y. Cheng, Z. Chen, R. Yang, G. Zhao, Recent progress of mechanism of mineralization process induced by Ta2O5/PCL scaffolds, J. Appl. Polym. Sci. 139 (2022) e52649.
[61] K. Wu, X. Wu, J. Guo, Y. Jiao, C. Zhou, Facile Polyphenol-Europium Assembly Enabled Functional Poly(l-Lactic Acid) Nanofiber Mats with Enhanced Antioxidation and Angiogenesis for Accelerated Wound Healing, Adv. Healthc. Mater. 10 (2021) 2100793.
[62] J. Fang, T. Seki, H. Maeda, Therapeutic strategies by modulating oxygen stress in cancer and inflammation, Adv. Drug Deliv. Rev. 61 (2009) 290–302.
[63] T. Shimizu, Y. Nakanishi, M. Nakahara, N. Wada, Y. Moro-Oka, T. Hirano, T. Konishi, S. Matsugo, Structure Effect on Antioxidant Activity of Catecholamines toward Singlet Oxygen and Other Reactive Oxygen Species in vitro, J. Clin. Biochem. Nutr. 47 (2010) 181–190.
[64] Q. Zhong, G. Li, H. Long, J. Zhang, S. Deng, L. Huang, S. Tan, Smart DEA–QCGM–CNT hydrogels with temperature- and NIR-responsive behavior achieved by the synergy between CNT and QCGM for wound dressing, Mater. Adv. 3 (2022) 2568–2582.
[65] R. Lima-Sousa, D. de Melo-Diogo, C.G. Alves, C.S.D. Cabral, S.P. Miguel, A. G. Mendonça, I.J. Correia, Injectable in situ forming thermo-responsive graphene based hydrogels for cancer chemo-photothermal therapy and NIR light-enhanced antibacterial applications, Mater. Sci. Eng. C 117 (2020), 111294.
[66] C. Lin, D. Sheng, X. Liu, S. Xu, F. Ji, L. Dong, Y. Zhou, Y. Yang, NIR induced self-healing electrical conductivity polyurethane/graphene nanocomposites based on Diels−Alder reaction, Polymer 140 (2018) 150–157.
[67] G.M. Neelgund, M.C. Okolie, F.K. Williams, A. Oki, Ag2S nanocrystallites deposited over polyamidoamine grafted carbon nanotubes: An efficient NIR active photothermal agent, Mater. Chem. Phys. 234 (2019) 32–37.
[68] J. Zeng, L. Yang, Q. Liang, X. Zhang, H. Guan, X. Xu, X. Chen, X. Jing, Influence of the drug compatibility with polymer solution on the release kinetics of electrospun fiber formulation, J. Control. Release 105 (2005) 43–51.
[69] G.P. Mishra, V. Tamboli, A.K. Mitra, Effect of hydrophobic and hydrophilic additives on sol-gel transition and release behavior of timolol maleate from polycaprolactone-based hydrogel, Colloid Polym. Sci. 289 (2011) 1553–1562.
[70] F. Ouazib, N.B. Mokhnachi, N. Haddadine, R. Barille, Role of polymer/polymer and polymer/drug specific interactions in drug delivery systems, J. Polym. Eng. 39 (2019) 534–544.
[71] Q. Xiong, Q. Fang, K. Xu, G. Liu, M. Sang, Y. Xu, L. Hao, S. Xuan, Near-infrared light-responsive photothermal α-Fe2O3@Au/PDA core/shell nanostructure with on–off controllable anti-bacterial effects, Dalton Trans. 50 (2021) 14235–14243.
[72] C. Wan, B. Chen, Poly(ε-caprolactone)/graphene oxide biocomposites: mechanical properties and bioactivity, Biomed. Mater. 6 (2011), 055010.
[73] J. Balcucho, D.M. Narváez, J.L. Castro-Mayorga, Antimicrobial and Biocompatible Polycaprolactone and Copper Oxide Nanoparticle Wound Dressings against Methicillin-Resistant Staphylococcus aureus, Nanomaterials 10 (2020) 1692.
[74] K. Aoki, N. Saito, Biocompatibility and carcinogenicity of carbon nanotubes as biomaterials, Nanomaterials 10 (2020) 264.
[75] P. Feng, M. Liu, S. Peng, S. Bin, Z. Zhao, C. Shuai, Polydopamine modified polycaprolactone powder for fabrication bone scaffold owing intrinsic bioactivity, J. Mater. Res. Technol. 15 (2021) 3375–3385.
[76] J. Li, L. Li, J. Zhou, Z. Zhou, X.-L. Wu, L. Wang, Q. Yao, 3D printed dual-functional biomaterial with self-assembly micro-nano surface and enriched nano argentum for antibacterial and bone regeneration, Appl. Mater. Today 17 (2019) 206–215.
[77] W. Wang, G. Caetano, W.S. Ambler, J.J. Blaker, M.A. Frade, P. Mandal, C. Diver, P. Bártolo, Enhancing the Hydrophilicity and Cell Attachment of 3D Printed PCL/Graphene Scaffolds for Bone Tissue Engineering, Materials 9 (2016) 992.
[78] D. Kumar, G. Babu, S. Krishnan, Study on mechanical & thermal properties of PCL blended graphene biocomposites, Polímeros 29 (2019).
[79] M.B. Hajduga, R. Bobiński, M. Dutka, I. Ulman-Włodarz, J. Bujok, C. Pająk, M. Ćwiertnia, A. Kurowska, M. Dziadek, I. Rajzer, Analysis of the antibacterial properties of polycaprolactone modified with graphene, bioglass and zinc-doped bioglass, Acta Bioeng. Biomech. 23 (2021) 131–138.
[80] M. Mahmoodi, V. Haghighi, M. Mirhaj, M. Tavafoghi, F. Shams, A. Darabi, Highly osteogenic and mechanically strong nanofibrous scaffolds based on functionalized multi-walled carbon nanotubes-reinforced electrospun keratin/poly (ε-caprolactone), Mater. Today Commun. 27 (2021), 102401.
[81] S. Evlashin, P. Dyakonov, M. Tarkhov, S. Dagesyan, S. Rodionov, A. Shpichka, M. Kostenko, S. Konev, I. Sergeichev, P. Timashev, I. Akhatov, Flexible Polycaprolactone and Polycaprolactone/Graphene Scaffolds for Tissue Engineering, Materials (Basel) 12 (2019) 2991.
[82] L. Ferroni, C. Gardin, F. Rigoni, E. Balliana, F. Zanotti, M. Scatto, P. Riello, B. Zavan, The Impact of Graphene Oxide on Polycaprolactone PCL Surfaces: Antimicrobial Activity and Osteogenic Differentiation of Mesenchymal Stem Cell, Coatings 12 (2022) 799.
[83] S. Faraji, N. Nowroozi, A. Nouralishahi, J. Shabani Shayeh, Electrospun poly-caprolactone/graphene oxide/quercetin nanofibrous scaffold for wound dressing: Evaluation of biological and structural properties, Life Sci. 257 (2020), 118062.